

12-31-2019

Micro pipes – a portable integrated platform for electrochemical sensing using essence architecture

Hansin Kim
New Jersey Institute of Technology

Follow this and additional works at: <https://digitalcommons.njit.edu/theses>



Part of the [Biomedical Engineering and Bioengineering Commons](#)

Recommended Citation

Kim, Hansin, "Micro pipes – a portable integrated platform for electrochemical sensing using essence architecture" (2019). *Theses*. 1741.

<https://digitalcommons.njit.edu/theses/1741>

This Thesis is brought to you for free and open access by the Electronic Theses and Dissertations at Digital Commons @ NJIT. It has been accepted for inclusion in Theses by an authorized administrator of Digital Commons @ NJIT. For more information, please contact digitalcommons@njit.edu.

Copyright Warning & Restrictions

The copyright law of the United States (Title 17, United States Code) governs the making of photocopies or other reproductions of copyrighted material.

Under certain conditions specified in the law, libraries and archives are authorized to furnish a photocopy or other reproduction. One of these specified conditions is that the photocopy or reproduction is not to be “used for any purpose other than private study, scholarship, or research.” If a user makes a request for, or later uses, a photocopy or reproduction for purposes in excess of “fair use” that user may be liable for copyright infringement,

This institution reserves the right to refuse to accept a copying order if, in its judgment, fulfillment of the order would involve violation of copyright law.

Please Note: The author retains the copyright while the New Jersey Institute of Technology reserves the right to distribute this thesis or dissertation

Printing note: If you do not wish to print this page, then select “Pages from: first page # to: last page #” on the print dialog screen

The Van Houten library has removed some of the personal information and all signatures from the approval page and biographical sketches of theses and dissertations in order to protect the identity of NJIT graduates and faculty.

ABSTRACT

μ PIPES – A PORTABLE INTEGRATED PLATFORM FOR ELECTROCHEMICAL SENSING USING ESSENCE ARCHITECTURE

**by
Hansin Kim**

The field of microfluidics and lab-on-chip (LOC) technology has the potential to have a truly transformative effect in biological engineering. This includes areas such as single-cell analysis, environmental monitoring, regenerative medicine, and point-of-care diagnostics. Yet despite being the subject of intense research over the past two decades, LOC devices have not been widely adopted. It is increasingly evident that there is a need for an effective and adaptable integration strategy to realize the potential of this technology.

Presented in this thesis is a design for a chip-to-world interface that aims to improve integration while maintaining cost-efficiency and ease of fabrication. This was achieved chiefly by using 3D printing to produce components that fit together precisely, minimizing the need for fasteners or adhesives during assembly. An accompanying LabVIEW program was written to automate some of the functions of the microfluidic device.

Experiments were then conducted to evaluate the integrity efficacy of the interface. First, solutions of food colorant dye and then fluorescent dye were passed through the chip to test for leaks. Electrochemical impedance spectroscopy (EIS) was then used to take readings of three different solutions, potassium chloride (KCl), DNA, and phosphate-buffered saline (PBS), to test the responsiveness of the system and to evaluate its effectiveness as a biosensor.

The interface performed satisfactorily in all experiments, demonstrating its potential as an effective step towards a fully integrated microfluidic device.

**μ PIPES – A PORTABLE INTEGRATED PLATFORM FOR
ELECTROCHEMICAL SENSING USING ESSENCE ARCHITECTURE**

**by
Hansin Kim**

**A Thesis
Submitted to the Faculty of
New Jersey Institute of Technology
in Partial Fulfillment of the Requirements for the Degree of
Master of Science in Biomedical Engineering**

Department of Biomedical Engineering

December 2019

APPROVAL PAGE

**μ PIPES – A PORTABLE INTEGRATED PLATFORM FOR
ELECTROCHEMICAL SENSING USING ESSENCE ARCHITECTURE**

Hansin Kim

Dr. Sagnik Basuray, Thesis Advisor Date
Assistant Professor of Chemical and Materials Engineering, NJIT

Dr. Max Roman, Committee Member Date
Professor of Biomedical Engineering, NJIT

Dr. Vivek A. Kumar, Committee Member Date
Assistant Professor of Biomedical Engineering, NJIT

Dr. Roman S. Voronov, Committee Member Date
Assistant Professor of Chemical and Materials Engineering, NJIT

BIOGRAPHICAL SKETCH

Author: Hansin Kim
Degree: Master of Science
Date: January 2019

Undergraduate and Graduate Education:

- Master of Science in Biomedical Engineering,
New Jersey Institute of Technology, Newark, NJ, USA 2020
- Bachelor of Science in Biomedical Engineering,
Johns Hopkins University, Baltimore, MD, USA 2015

Major: Biomedical Engineering

This thesis is dedicated to my family for their unwavering support and love.

ACKNOWLEDGEMENT

I want to thank my thesis advisor, Dr. Sagnik Basuray, for inviting me to work with him. I will always appreciate the opportunity I had to participate in his research and his constant support. I would also like to extend my thanks to Dr. Vivek Kumar and Dr. Roman Voronov for being members of the committee as well as Dr. Max Roman for his advice and guidance throughout my studies at NJIT. I would also like to thank Yu Hsuan Cheng and Zhenglong Li for their invaluable help with my research. Finally, I would like to acknowledge and thank my parents for their support throughout my academic career.

TABLE OF CONTENTS

Chapter	Page
1 INTRODUCTION	1
1.1 Background	1
1.2 Objective	10
2 BACKGROUND INFORMATION	12
2.1 Physics of Microfluidics.....	12
2.1.1 Fluidic Parameters.....	13
2.1.2 The Navier-Stokes Equation	15
2.1.3 Volumetric Flow	17
2.1.4 Transport Processes in Microfluidic Systems	17
2.2 Microfluidic Devices.....	19
2.2.1 Sensor Modalities.....	19
2.2.2 Interconnect and Packaging	21
2.3 Point of Care Diagnostic Testing	22
3 DESIGN & FABRICATION.....	24
3.1 Design.....	24
3.1.1 Housing	24
3.1.2 Spring Probes	26
3.1.3 Enclosure.....	29
3.2 Fabrication.....	30

TABLE OF CONTENTS
(Continued)

Chapter	Page
4 LABVIEW	32
4.1 Features of LabVIEW.....	32
4.2 Front Panel.....	33
4.2.1 Serial Communication	34
4.2.2 Pumping Parameters	34
4.2.3 Operating Controls.....	36
4.2.4 Indicators.....	36
4.3 Back Panel	37
4.3.1 Initialization Module.....	37
4.3.2 Pumping Parameter Module.....	38
4.3.3 Operations Module.....	39
4.3.4 Termination Module	41
5 MATERIALS AND METHODS.....	43
5.1 Materials	43
5.1.1 Glass Slides.....	43
5.1.2 Adhesive Tape	43
5.1.3 Deionized Water	44
5.1.4 Food Colorant	45
5.1.5 Fluorescein.....	45
5.1.6 Potassium Chloride.....	45

TABLE OF CONTENTS
(Continued)

Chapter	Page
5.1.7 Probe and Target DNA	45
5.1.8 Functionalization Reagents	46
5.1.9 Phosphate Buffered Saline	46
5.1.10 Carbon Nanotubes	46
5.2 Apparatus	47
5.2.1 Cricut Explorer®	47
5.2.2 NE-1000 Syringe Pump	48
5.2.3 Drill Press	49
5.2.4 Fluorescence Microscope	49
5.3 Device Fabrication	50
5.4 Food Colorant Run Protocol	51
5.5 Fluorescence Microscopy Protocol	51
5.6 Flow Rate Validation Protocol	52
5.7 KCl Run Protocol	53
5.8 Target DNA Run Protocol	54
5.9 PBS Experimental Protocol	55
6 RESULTS	57
6.1 Food Colorant Run	57
6.2 Fluorescence Microscopy	57
6.3 Flow Rate Validation	60

TABLE OF CONTENTS
(Continued)

Chapter	Page
6.4 KCl Run.....	61
6.5 Target DNA Run	62
6.6 PBS Run	66
7 CONCLUSION	74
8 FUTURE WORK.....	76
APPENDIX A LABVIEW BLOCK DIAGRAMS.....	78
A.1 Initialization module.....	78
A.2 Parameters module	79
A.3 Operations module (first half)	80
A.4 Operations module (second half).....	81
A.5 Termination module	82
REFERENCES.....	83

LIST OF TABLES

Table		Page
1.1	Summary of Experiments	11
2.1	Examples of Sensing Techniques Grouped by the Transducer	20
5.1	Parameters of Flow Rate Validation Experiments.....	53
5.2	Description of Electrode Configuration.....	53
5.3	Parameters of PBS Experiments.....	55
6.1	Mean, Minimum, and Maximum Intensity Values of Fluorescence Images.....	58
6.2	Summary of the Results of the Flow Rate Validation	60

LIST OF FIGURES

Figure		Page
1.1	Illustration of laminar and turbulent flow	1
1.2	Illustration of a typical photolithography process.....	2
1.3	Photograph of the first microscale gas chromatography system.....	4
1.4	Growth of publications of articles related to lab-on-chip	8
2.1	Schematic model of viscosity.....	14
3.1	Model of housing at various stages of design	26
3.2	An optical microscopic image of flat gold electrode showing effects of shear on gold electrodes following successive probing	27
3.3	Cross-section of the holder showing embedded spring probes	28
3.4	Model of the slider showing embedded spring probes.....	29
3.5	Model of the chip inserted into holder and assembled in enclosure	29
3.6	ED1055-ND spring probe	30
3.7	Photograph of assembled housing with chip.....	31
4.1	The front panel of the Pump Control VI	33
4.2	Serial communication controls.....	34
4.3	Pumping parameter controls	35
4.4	Operating controls	36
4.5	Indicators.....	37
4.6	Block diagram of the initialization module.....	38
4.7	Block diagram of the pumping parameter module.....	39
4.8	Marked block diagram of the operations module	41

4.9	Block diagram of the termination module after completion of a successful pumping sequence and after an error occurs	42
5.1	Cross-section of layers of adhesive tape	44
5.2	Milli-Q Direct 8 used to produce DI water	44
5.3	Red food colorant diluted in DI water.....	45
5.4	Cricut Explore® cutting machine with a cutting mat inserted.....	47
5.5	NE-1000 Syringe Pump	48
5.6	Olympus microscope with attached Hamamatsu digital camera	49
5.7	Fluorescence filter block of Olympus microscope.....	50
5.8	Electrode configurations for the ESSENCE microfluidic device	53
6.1	Photograph of unpacked chip with food colorant	57
6.2	Fluorescence microscopy images of the microfluidic channel	58
6.3	Fluoresce images of the microfluidic channel following the application of threshold.....	59
6.4	EIS spectra for multiple concentrations of KCl in an unpacked chip	61
6.5	EIS spectra for multiple concentrations of KCl in a packed chip	62
6.6	EIS spectra from target-DNA attachment to SWCNT with probe-DNA for ME configuration.....	64
6.7	EIS spectra from target-DNA attachment to SWCNT with probe-DNA for WE configuration.....	64
6.8	EIS spectra from target-DNA attachment to SWCNT with probe-DNA for ME and WE configuration.....	65
6.9	The plot of impedance over time for Run 1	66

6.10	Non-normalized mean impedances and standard deviations (represented as error bars) for PBS Run 1	67
6.11	Normalized standard deviations for PBS Run 1	68
6.12	The plot of impedance over time for Run 2	69
6.13	Non-normalized mean impedances and standard deviations (represented as error bars) for PBS Run 2	70
6.14	Normalized standard deviations for PBS Run 2	70
6.15	The plot of impedance over time for Run 3	71
6.16	Non-normalized mean impedances and standard deviations (represented as error bars) for PBS Run 3	72
6.17	Normalized standard deviations for PBS Run 3	72

CHAPTER 1

INTRODUCTION

1.1 Background

Microfluidics is the field of study that investigates the behavior, control and manipulation of small amounts of fluid at the micrometer or nanometer scale (Chen et al., 2010; Whitesides, 2006).

The significance of this reduction to the microscale cannot be overstated. At the length scales considered in microfluidics the physical behavior of fluids differs significantly from that of the macroscopic world of everyday experience. For example, gravitational forces become negligible at the microscale because the amount of liquid used is so minute. Instead forces like surface tension and viscosity become predominant (Squires & Quake, 2005). Another noteworthy difference is how fluids move at the microscale. At the macroscale, the flow is in the turbulent regime wherein fluid motion is characterized by chaotic changes in pressure and velocity. This chaotic motion creates eddies or packets of fluid particles that result in lateral mixing. At the microscale, the flow enters the laminar regime wherein fluid particles move smoothly in infinitesimal parallel layers (laminae). Each layer slides past adjacent layers with little or no mixing.

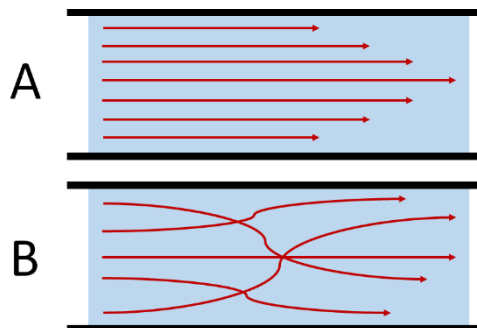


Figure 1.1 A – Illustration of laminar flow, B – Illustration of turbulent flow.

The practical upshot is that these phenomena can be leveraged by microfluidic systems to yield useful outcomes such as reduced reagent consumption, shortened assay times, reduced power requirements, and parallelization (A. J. Chung, Kim, & Erickson, 2008; Hettiarachchi, Talu, Longo, Dayton, & Lee, 2007; Rohde, Zeng, Gonzalez-Rubio, Angel, & Yanik, 2007; Sista et al., 2008). More detailed discussion of phenomena that affect microfluidic systems are included in section 2.1.

The origins of microfluidics as a field can be traced back to the development of microelectronics. In 1947, Willian Shockley, Walter Brattain, and John Bardeen of Bell Telephone Laboratories invented the first transistor, originally intended to support the mechanical relay systems of telephone lines (Jr, 2001). In 1952, the need to miniaturize electronic components to fit within a limited space prompted Lathrop and Nall to develop the technique of photolithography wherein a light-sensitive photoresist is used as a mask to shield areas of a substrate material from a subsequent etching process (Lathrop, 2013).

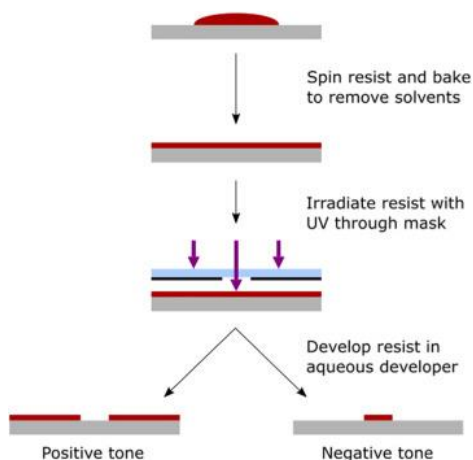


Figure 1.2 Illustration of a typical photolithography process. A photoresist material is spin-coated to distribute evenly over a substrate to the desired thickness. The resist is irradiated with UV light through a photomask. For positive resists, areas not exposed to UV radiation are removed by dissolving or etching while the opposite is true for negative resists.

Source: Convery, N., & Gadegaard, N. (2019). 30 years of microfluidics. *Micro and Nano Engineering*, 2, 76-91. doi:<https://doi.org/10.1016/j.mne.2019.01.003>.

Photolithography techniques would become the standard in microelectronic manufacturing and made large-scale parallel production possible. Jack Kilby at Texas Instruments would later refine this work in a 1964 patent that demonstrated how multiple discrete electronic components such as transistors, resistors and capacitor could be manufactured on an individual silicon crystal (Kilby, 2000). This was the first-ever integrated circuit (IC) and would trigger a revolution in microelectronics.

Another new technology that contributed to the emergence of microfluidics was also developed at this time: inkjet printing. Though it was first realized in a working device by Richard Sweet in 1964, the theory behind it was first described by Walter Rayleigh nearly a century prior. In his 1879 paper, Rayleigh described how a falling stream of fluid breaks into discrete droplets to minimize surface area and thus surface energy (Strutt, 1879). Sweet harnessed this phenomenon by forcing ink through a small, vibrating nozzle 35 μm in diameter (Sweet, 1965). As ink exited the nozzle, it formed into discrete droplets which were then charged by an electrode. The droplets were then passed through an electric field, which deflected the drop depending on their charge. As a paper was moved underneath the jet, the deflected droplets formed a pattern that could be used to determine the charge on each individual drop with respect to time. This oscillograph is considered to be the first microfluidic device. Bassous et al. at IBM would further advance inkjet printing by using photolithography to fabricate an array of nozzles on an individual silicon wafer (Bassous, Taub, & Kuhn, 1977). While the more obvious effect of this innovation was to make inkjet printers more affordable for the average consumer, it also demonstrated that photolithography of silicon material could be used to mass-produce microfluidic devices.

As photolithographic and etching techniques continued being refined, interest grew in using these techniques outside the realm of electronics. Molecular chemical analysis was the first field to benefit from the application of microelectronic manufacturing approaches. The intention was to minimize the fluid systems of existing devices to create smaller, more robust equipment.

This work was first carried out by Terry et al. at Stanford University and in 1979 they published a paper detailing the creation of a microscale gas chromatography system on a 5cm silicon wafer (Terry, Jerman, & Angell, 1979). By applying the same photolithography and etching techniques used to design and manufacture microelectronics, they were able to create an injection valve joined to a 1.5m long capillary coil that ended in a thermal conductivity sensor.

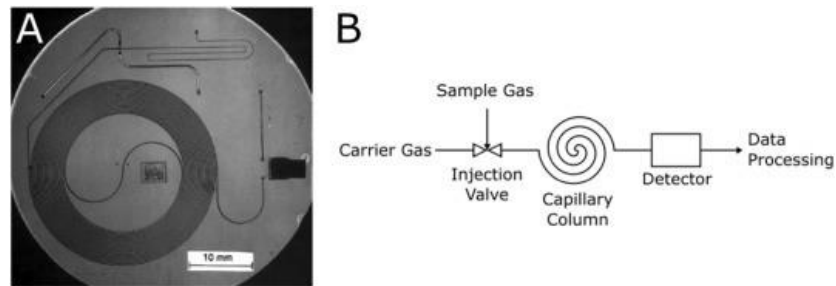


Figure 1.3 A - Photograph of gas chromatography system as described by Terry et al. Device consists of 1.5m long, spiral capillary column with input (top right) and exhaust (right) for gas sample. Flow within the device is controlled with a valve (top left) before the capillary coil and the detector is visible to the right of the device. B – Schematic showing fluid handling components.

Source: Terry, S. C., Jerman, J. H., & Angell, J. B. (1979). A gas chromatographic air analyzer fabricated on a silicon wafer. *IEEE Transactions on Electron Devices*, 26(12), 1880-1886. doi:10.1109/T-ED.1979.19791.

This detector could provide a highly sensitive and specific analysis of the composition of an injected gas mixture. Moreover, it was determined that reducing the

cross-sectional area of the capillary had led to an increase in the performance of the device, demonstrating the value of a microsystem for analysis. Additionally, the valve design had a dead volume of approximately 4 nl and was capable of injecting volumes of gas as small as 1 nl into the capillary, showing how reducing the dimensions of the device also resulted in correspondingly reduced reagent consumption while maintaining comparable performance to much bulkier techniques that were the standard. This publication is now considered a seminal work and the start of microfluidics as a separate field of its own.

The gas chromatography system developed by Terry et al. is also considered to be the first example of a “micro total analysis system” (μ TAS), though the term was not in use at the time. For the past twenty years, there has been an increasing demand for continuous and fast-response measurements using small volumes and low concentration samples. This has been a driving force for research in many areas of analytical chemistry. One possible solution to satisfy these needs is the total analysis system (TAS) approach. Ideally, a TAS would perform all the component stages of analysis in an integrated and automated fashion while maintaining high sensitivity and selectivity necessary for the detection of tiny amounts of analytes in complex sample mixtures. These component stages could include sampling, pre-treatment, chemical reactions, separations analyte detection, product isolation and data analysis. Manz et al. would later extend this idea into the concept of μ TAS wherein these integrated and automated systems would be miniaturized into a device that would measure only square millimeters to square centimeters in size (Manz, Graber, & Widmer, 1990).

Micro total analysis systems, sometimes referred to as lab-on-chip (LOC) devices, have grown substantially and expanded into a more general area of research beyond

analytical chemistry (Dittrich, Tachikawa, & Manz, 2006). It now includes many different types of microfabricated chemical, biochemical and biological systems. The objective of these microfluidic systems is to automate laboratory processes and to conduct chemical/biochemical analysis in a significantly miniaturized format (Mark, Haeberle, Roth, von Stetten, & Zengerle, 2010). As mentioned above, the speed and cost-efficiency, small reagent consumption and less waste generation are obvious advantages. Furthermore, the results of the analysis could be obtained within a few seconds, instead of hours or days (Schneider, 2018).

In recent years, microfluidics and LOC have undergone rapid development with numerous new fabrication techniques and novel device designs emerging every year. Since the late 1990s, an increasingly large number of publications and patents of microfluidic devices have been released. These microscale devices now have functionality as pumps (Huang, Wu, Cui, Cui, & Lee, 2008; Jeong & Konishi, 2008; Ryu, Chung, & Cho, 2010), mixer (Mansur, Ye, Wang, & Dai, 2008; Nguyen & Wu, 2005; Ward & Fan, 2015), concentrators (Choi & Chae, 2010), and valves (Churski, Michalski, & Garstecki, 2010; Kaigala, Hoang, & Backhouse, 2008; Kim, Chen, & Bau, 2009; Unger, Chou, Thorsen, Scherer, & Quake, 2000) Such components are vital building blocks for creating functional lab-on-chip systems. There has also been increasing interest in the potential application of LOC technology for point-of-care (POC) testing (Chin, Linder, & Sia, 2007). Point-of-care diagnostic systems are instruments that rapidly provide *in vitro* diagnostic results (Tudos, Besselink, & Schasfoort, 2001). A report by the National Institutes of Health suggests that the widespread adoption of competent, reliable POC testing could trigger a paradigm shift from curative to predictive, personalized and preemptive medicine (Gomez, 2013).

Under the current arrangement diagnostic tests are performed in a central laboratory using bench-top analytical equipment operated by trained personnel (Ng & Wheeler, 2015). Thus, a patient must first visit a clinic or hospital where samples are taken, the samples must be sent to the laboratory and analyzed, and the results sent back. The entire process requires patients to wait days before actually receiving their test results, delaying treatment and possibly prolonging illness. In resource-limited settings, the turnaround time may be even longer. Consequently, there has been a growing interest in POC testing to shift away from traditional diagnostics in the clinical laboratory to near-patient settings. Ideally, the test results are presented in a manner that can be understood by non-trained personnel at a patient site in the physician's office, the field, the home, an ambulance, or a hospital and provide results immediately (Paul Yager et al., 2006).

A capable POC device would provide physicians with more timely diagnostic information to make better-informed decisions regarding diagnosis and treatment, especially with regards to treating acute illnesses (Wang, Inci, De Libero, Singhal, & Demirci, 2013). Patients would also be empowered by the ease of use of POC devices as they will allow them to evaluate their health quantitatively at home. This is especially relevant for chronic diseases such as diabetes monitoring. Making diagnostic devices that are more cost-effective, portable, and operable by non-experts would also help make healthcare more accessible in remote communities or developing nations.

The essential features for modern POC diagnostics are (1) quick analysis time such that patients may immediately receive follow-up treatment at the point-of-care; (2) high sensitivity with accurate results comparable to those of conventional bench-top analyzers; and (3) easy-to-use "sample-to-answer" format. The latter feature means that the device

requires only that the user insert a sample and does not require further input, thereby making the device accessible even to non-experts (Nayak, Blumenfeld, Laksanasopin, & Sia, 2017). Microfluidic LOCs are quite promising for this application since they can operate using minute (microliter or picoliter) volumes of the sample fluid and can integrate some or all analytical steps such as sample pretreatment, reaction, separation and detection (P. Yager, Domingo, & Gerdes, 2008).

Yet despite their promise, LOC technology has not been widely adopted in biological engineering or medical applications. Interest in LOC remains high, as evidenced by the steadily increasing number of publications related to the technology (see **Figure 1.4** below), but the very few devices have reached the commercial market. Existing microfluidic systems remain confined to research laboratories rather than in the field or hospitals (Jungkyu Kim et al., 2009). At present, the most successful portable bioanalytical platforms to reach the market are paper-based test strips, first introduced in the mid-1980s (Posthuma-Trumpie, Korf, & van Amerongen, 2009).

The simplicity of the test strip is its most significant advantage. Liquid transport is driven by capillary action, eliminating the need for external pumps or fluid transport. As the sample fluid is drawn through the strip, it comes into contact with reagent molecules pre-immobilized on the strip (Yang et al., 2018). The strip can also be used as an effective filter, a vital feature for processing physiological samples. The rate of uptake can also be manipulated by altering the permeability, roughness, dimension or surface properties of the paper material. That features can be integrated into a compact package without the need for additional equipment makes test strips highly portable and cost-effective, making them

ideal for point-of-care diagnostics such as cardiac marker assays or pregnancy tests (Sharma, Zapatero-Rodríguez, Estrela, & O'Kennedy, 2015).

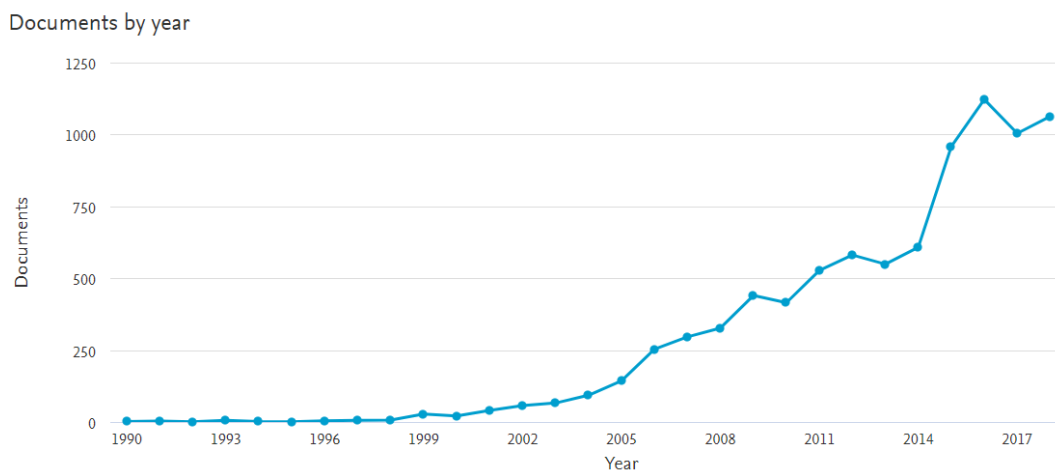


Figure 1.4 Growth of publications of articles related to lab-on-chip from 1990 to 2018

Source: Scopus, search for topic “lab on chip”, <https://www.scopus.com>.

In contrast to the success of the test strip, a significant challenge is restricting microfluidic devices from transforming into truly practical solutions for the laboratory or commercial marketplace. That challenge is the need to integrate a variety of disparate components into a fully automated platform. Current devices are more “chip-in-lab” than “lab-on-chip” and are often internally designed and fabricated for the particular needs of a given laboratory, frustrating efforts to standardize microfluidics in the same manner as microelectronics (Mohammed, Haswell, & Gibson, 2015). This is primarily due to the engineering difficulties inherent in combining such a diverse array of components and functions including bulky supporting devices (e.g. pressure sources and cell culture reservoirs), sensor and detector systems (e.g. optical or electrical interfaces), and sample

preparation modules (e.g. mixers and concentrators) into a single compact device (Kuo & Chiu, 2011).

1.2 Objective

The goal of this thesis is to present and experimentally validate a design for a simple, easy-to-build, cost-effective interface for a microfluidic device as well as accompanying software to automate the operation of a connected pump. The interface was designed in Creo Parametric and manufactured from PLA plastic by 3D printing which dramatically reduces overall cost. The use of 3D printing also has the benefit of allowing for easy customization or alteration to the design as parameters change. The various electrical and fluidic connections were realized using off-the-shelf components, further simplifying the design and helping maintain a low cost.

The chip itself is placed within a housing that serves to both hold the chip securely and align on-chip components to interconnects on the housing. A series of spring probes are incorporated into the housing to achieve reversible electrical connections that automatically contact the electrode pads on the chip.

A NE-1000 syringe pump drives the fluidic components. The pump can be programmed to execute a pumping protocol, but this requires the use of extremely unintuitive controls to input commands. A program was developed in the LabVIEW programming environment that allows an investigator to input pumping parameters into a user-friendly graphical user interface. This pumping program automates control of the syringe pump and reduce the need for manual handling of the fluidic components. This has the benefit of freeing a researcher to focus on sampling data rather than pausing to adjust

the pump manually. Experiments were then conducted to check for leaks and to validate that the stability and sensitivity of the electrical connections were comparable to standard electrical connections.

Table 1.1 Summary of Experiments

Experiment	Description
1 - Food colorant	A solution of food colorant is passed through an empty chip as a simple visual inspection for leaks.
2 - Fluorescence microscopy	A solution of fluorescein dye is passed through an empty chip; fluorescence microscopy is used to image the microfluidic channel; the images captured are thresholded as a quantitative check for leaks.
3 - Potassium chloride (KCl)	Solutions of KCl of varying concentration are passed through an empty chip; electrochemical impedance spectroscopy (EIS) is used and the resulting spectra compared to spectra captured in a previous experiment conducted by Cheng et al.
4 – Flow rate validation	A syringe pump is used to dispense a set volume of DI water through an unpacked chip at various flow rates. After the fluid is dispensed, the volume is measured and used to calculate an actual flow rate. This is to confirm that the flow rate registered on the pump is indeed the actual flow rate.
5 - Target DNA	A chip is packed with carbon nanotubes (CNT) functionalized with probe-DNA; a solution of complementary target-DNA is passed through the packed chip; two different electrode configurations are used as described in a previous experiment conducted by Cheng et al. EIS is used and the resulting spectra compared to spectra captured by Cheng et al.
6 - Phosphate-buffered saline (PBS)	Two syringe pumps are prepared with PBS solutions of varying concentration. The two pumps alternate pumping at 20-minute intervals into an empty chip at varying flow rates and EIS readings are captured every 5 minutes. This tests if the EIS readings remain stable even as concentration and flow rate changes.

CHAPTER 2

BACKGROUND INFORMATION

The numerous advantages microfluidics offers researchers are the result of the drastically different behavior of fluids at the microscale. The most obvious difference is that the chaotic, turbulent flow observed in the macroscale, such as a river or water running from a faucet, is absent. Instead the flow is referred to as laminar flow. Another difference is that phenomena that dominate in one scale are diminished or negligible in the other. For example, the macroscale parameter of inertia becomes insignificant at the microscale while conversely, the viscosity becomes extremely important. In a similar vein, diffusion would be useless for transport on the macroscale yet becomes significant on the microscale. The surface of a microsystem must be considered more carefully as the surface-to-volume ratio (S/V) increases dramatically as a system is downscaled. A cubic macrosystem measuring 1 m on each side would have $S/V = 6 \text{ m}^{-1}$ while a system with sides of $1 \text{ }\mu\text{m}$ would have $S/V = 6,000,000 \text{ m}^{-1}$. In this chapter, the fundamental physics of microfluidic theory will be presented as well as a review of current LOC technology and POCT diagnostics.

2.1 Physics of Microfluidics

In contrast to the molecules of solids, molecules in a fluid have comparatively larger spaces between molecules and hence have greater freedom of movement. Indeed, a fluid is defined as a material that deforms continuously under shear stress. In fluid mechanics, a fluid is considered to exist in a continuum wherein the average parameters examined as opposed to the parameters of any individual molecule. This approximation holds for most

microfluidic systems as the properties under consideration are on the length scale of ~10 micrometers.

2.1.1 Fluidic Parameters

This section will discuss parameters that are important for describing fluids, with a particular emphasis on what happens to them on the microscale. The most important parameters for characterizing a fluid are density (ρ), pressure (P) and viscosity (η). The density of a liquid is defined as mass (m) per unit volume (v).

$$\rho = \frac{m}{v} \quad (2.1)$$

The pressure of a liquid is only dependent on depth and is not relevant in a closed microfluidic system. In open microfluidic systems, a pressure difference induced externally will affect the flow of the liquid in the system. Pressure (P) is the ratio of the force applied (F) to the area (A) over which the force is distributed. In microfluidic systems a reservoir can be used to manipulate the pressure and by extension the flow rate.

$$P = \frac{F}{A} \quad (2.2)$$

Viscosity (η) acts as a resistance to flow in a system and is calculated as a ratio of shear stress to shear rate. A simple model of viscosity is displayed in Fig. 2.1. Two parallel plates are positioned a distance L apart and are filled with a liquid. If the upper plate is moved by a force F and results in a velocity v , then the liquid will experience a movement

as well. The layer of liquid immediately adjacent to the moving plate will be set into motion. This movement is then transferred by momentum to the next layer and so on. Under steady-state conditions, the velocities of these layers will range from v adjacent to the upper plate to 0 adjacent to the stationary lower plate.

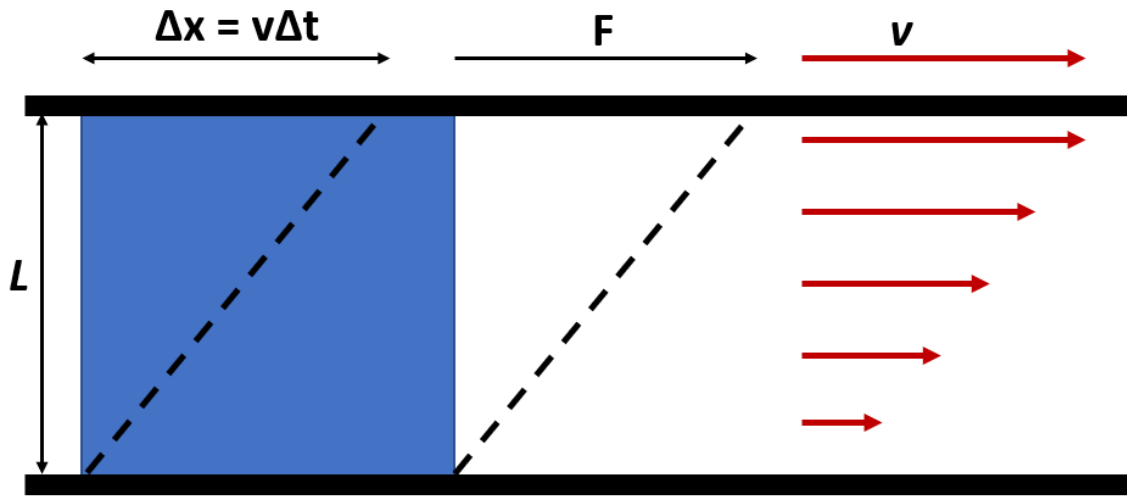


Figure 2.1 Schematic model of viscosity.

The shear stress is given as a ratio of the force F acting on the cross-sectional area A that lies parallel to the force.

$$\text{Shear stress} = \frac{F}{A} \quad (2.3)$$

The shear rate is given as the ratio of the velocity v to the distance L between the plates.

$$\text{Shear rate} = \frac{v}{L} \quad (2.4)$$

Assuming that velocity varies linearly with position, the viscosity is then given by:

$$\eta = \frac{F/A}{v/L} \quad (2.5)$$

Examining these simple parameters already yields some information about the flow in microsystems. For example, the ratio of inertial forces to viscous forces produces a dimensionless number called the Reynolds number which can be used to define the type of flow expected in the system (Reynolds, 1883). The Reynolds number is given by:

$$Re = \frac{\rho dv}{\eta} = \frac{dv}{\nu} \quad (2.6)$$

Note that d represents the characteristic linear dimension of the system, such as the diameter of tubes or the width/height of a rectangular channel. When the Reynolds number exceeds 4,000, the turbulent flow regime occurs while at Re less than 2,300 the laminar flow regime dominates. In general, flow in microsystems is always laminar. This is advantageous because the laminar flow is highly predictable, making mathematical modeling of such systems less intensive. Furthermore, molecular transport differs in the laminar flow as opposed to the turbulent flow in that there is no convective mixing. Instead, there is only diffusion, which also lends itself to predictable kinetics and can be easily represented mathematically.

2.1.2 The Navier-Stokes Equation

The Navier-Stokes equation is derived from fundamental laws of conservation. It begins with an equation of motion that is itself a rewritten form of Newton's 2nd law:

$$M d_t v = \sum_j F_j \quad (2.7)$$

In this equation d_t represents the total time derivative. There is also a sum of forces acting on the mass M and changing its velocity v in time. However, while working with fluids, it is densities rather than masses that are considered. Thus, it is necessary to divide by the volume V to obtain the following modified form:

$$\rho D_t v = \rho(\partial_t v + v \cdot \nabla v) = \sum_j f_j \quad (2.8)$$

What results is the fluid density $\rho = m/V$ and so-called “force densities” \mathbf{f}_j with D_t being the material time derivative. The latter can be further rewritten as $D_t = \partial_t + v \cdot \nabla$. The above equation can now be conceptualized as the forces acting on a particle of fluid and changing its velocity as it flows along with the surrounding field.

The most common force densities within microfluidic systems are: (1) from changes in pressure p : $f_{pressure} = -\nabla p$ and (2) from the viscosity of the fluid: $f_{viscosity} = \eta \nabla^2 v$. Thus **Equation 2.8** may be rewritten to produce the Navier-Stokes equation for incompressible fluids:

$$\rho(\partial_t v + v \cdot \nabla v) = -\nabla p + \eta \nabla^2 v \quad (2.9)$$

2.1.3 Volumetric Flow

In microfluidics, it is common to use the parameter of volumetric flow rate, expressed as $Q = \Delta V/t = (\text{mean velocity}) \times (\text{cross-sectional area})$ which can be written as:

$$Q = \frac{\pi R^4}{8\eta L} \Delta P \quad (2.10)$$

The reciprocal term $8\eta L/\pi R^4$ is called the hydraulic resistance R_{Hyd} . The dependence on $1/R^4$ indicates the fluidic resistance increases rapidly as the dimensions are reduced and therefore higher pressure is required to drive fluid through the channels.

2.1.4 Transport Processes in Microfluidic Systems

The modes of transport in microfluidic systems can be broadly divided into direct and statistical transport mechanisms (Yildiz-Ozturk & Yesil-Celiktas, 2015). Direct transport is where fluid movement is controlled by applying work on the fluid, creating a flow with a direction and velocity profile. The work can be from a manual source such as pressure from a pump or electrically by electroosmotic flow. In contrast, statistical flow is transport driven by entropy, meaning the fluid is more disordered after the flow has occurred. Diffusion is the most familiar example of an analytical transport process. For microsystems the three most important processes are advection, migration and diffusion (Ward & Fan, 2015).

Advection is the transport of matter due to the bulk motion of a fluid in a particular direction. Free advection is when no external forces are applied. Forced advection is when fluid is moved due to an applied external force driving a directed flow.

Migration is the transport of matter in response to an electrical field. This is a conventional means of manipulating fluids in microsystems because the target molecules are ionized in a polar liquid such as water and thus an electrical field applied to the system can direct the fluid, moving the target molecules along with it.

Diffusion is defined as the stochastic process by which molecules drift from one region to another (Luka et al., 2015). Each molecule moves in one direction until another molecule hits it and this collision will cause a change in direction. No net flow is observable, but mixing can occur. The statistical nature of movement due to diffusion is described as a random walk. The following equation can approximate diffusion time in a single dimension:

$$t \approx \frac{x^2}{2D} \quad (2.11)$$

Here x represents the average distance travelled by a single molecule of solute in one dimension after time t while D is the coefficient of diffusion of said solute. D is an expression of how fast a concentration diffuses at a difference. It can be seen that the time is proportional to the distance squared. Therefore, as the scale of a given system is reduced and distances are shortened, the time required for molecules to travel across it by diffusion is reduced. This property is especially important for larger molecules that have lower diffusion coefficients such as DNA, as transport by diffusion alone will be significantly slower.

Because the directed and statistical transport mechanisms are very different, it is useful to compare them against each other. The Péclet number Pe describes the ratio of advective to diffusive transport of molecules in a fluid and is given by:

$$Pe = \frac{vL}{D} \quad (2.12)$$

In this equation, D is the coefficient of diffusion while v and L are the characteristic velocities and characteristic length of the system. In this case, the length refers to the distance over which advection and diffusion occur. As the Péclet number increases, diffusion becomes less important. Thus, for smaller ions diffusion is a relatively fast process but for larger species of molecule such as DNA, relying only on diffusive processes will require much longer timeframes (Ward & Fan, 2015).

2.2 Microfluidic Devices

2.2.1 Sensor Modalities

The sensor element in a microfluidic device may be categorized into different types according to the nature of the transducer used (Luka et al., 2015). In the case of LOC devices, the transducer transforms a relevant biomolecule-analyte into a measurable optical or electrical signal. The choice of transducer depends on the nature of the physicochemical change of the reaction that occurs at the sensing layer. A wide range of transducers has been developed over the years, such as optical (including colorimetric), piezoelectric, magnetic, and electrochemical.

Table 2.1 Examples of Sensing Techniques Grouped by the Transducer

Transducer	Technique	Advantages	Disadvantages
Optical	Surface plasmon resonance (SPR) (Guo, 2012)	Real-time detection; reliable, high sensitivity	Sensitive to the surrounding environment, requires bulky optical components
Mechanical	Cantilever (Liu et al., 2013)	Real-time detection; detect multiple analytes with high sensitivity	Sensitive to the surrounding environment, temperature
	Quartz crystal microbalance (C. Cheng, Chang, & Chu, 2011)	Real-time detection, simplicity, suitable for POCT devices	Sensitive to the surrounding environment, temperature and physical stress
Electrochemical	Amperometric (Shi & Ma, 2011)	Simplicity, low cost	Sensitive to the surrounding environment, time-consuming
	Potentiometric (Zelada-Guillen et al., 2013)	Real-time detection	Sensitive to the surrounding environment, time-consuming,
	Impedimetric (Guo et al., 2012)	Simplicity and real-time detection	Sensitive to the surrounding environment, bulky devices required

Of these, electrochemical-based approaches have been of particular interest in recent years. The combination of high sensitivity, low power requirements, low cost, and relatively simple instrumentation make electrochemical detection well-suited for microfluidic applications. These sensors detect changes in the electrochemical responses that occur during a reaction of interest and can operate on the parameters of current (amperometric), potential (potentiometric), and impedance (impedimetric).

Electrochemical impedance spectroscopy is of particular interest for this thesis as it is the method currently being explored in the New Jersey Institute of Technology's Opto and Microfluidics Laboratory. Although EIS sensors are capable of producing rapid results and are cost-effective, they typically exhibit poor sensitivity which makes them poorly

suited for detecting biomolecules. While it is possible to improve the conductance of an EIS sensor by the addition of carbon-based transducers, the parasitic capacitance of the electric double layer will reduce sensitivity and increase noise. A recent publication by Cheng et al. demonstrated a protocol to pack a microfluidic channel with carbon nanotubes to increase convective transport while deterring the diffusive mechanics that give rise to the double layer (Y. H. Cheng et al., 2019). Note that it is the EIS data from this publication that will be used as a point of comparison with the EIS data presented later in this thesis.

2.2.2 Interconnect and Packaging

Interconnect technologies facilitate the efficient transport of samples from the macroscale to the microscale. These technologies are sometimes also referred to as “chip-to-world” or “world-to-chip” interfaces or “packaging” (Ghafar-Zadeh, Sawan, & Therriault, 2009).

Conventional approaches for delivering samples into a microfluidic device revolve around pressure-based seals from tubing inserted directly into holes punched or cut into PDMS devices or the use of adhesives. Another method is the manual insertion of a needle into a PDMS septum and the microfluidic device proper. More involved processes integrate the interconnects into the design of the microfluidic device, directly incorporating physical locking mechanisms that can make removable, tight, and high-pressure connections (J. Chung, Hwang, Chen, & Lee, 2018).

While the efficient delivery of samples has been invaluable to the advancement of LOC devices, there remain many challenges regarding the questionable reliability and lack of design flexibility (Barbier et al., 2006). For example, adhesive-based seals are reliable but require careful attention during positioning to avoid blocking channels or ports with adhesive. Gasket-type seals made by inserting tubing susceptible to leaks or in high-

pressure applications the tubing may be outright ejected from the openings in the device. Robust, multi-input systems do exist but require substantial effort, making a rapid redesign of the interconnect a daunting prospect when presented with highly specific parameters.

Stereolithography provides design flexibility and scalability but is limited to a particular material and result in rigid interconnects (Xu et al., 2017). A handful of commercial packaging methods do exist, but their costs can be prohibitive. Additionally, they are often intended to adhere to specific substrate materials such as silicon or glass. As a result, the microfluidics community often resorts to specific solutions made in-house that are either hand-made, fixed-design, or prohibitively expensive. This has contributed to confining LOC devices in the laboratory space as it is difficult for non-experts to adopt and effectively use them.

A microfluidic world-to-chip interconnect that is reliable, customizable, and user-friendly would make LOC devices far more accessible. This would not only go a long way towards improving research outcomes for a broader range of laboratories but also contribute significantly to the developing field of point-of-care diagnostics.

2.3 Point of Care Diagnostic Testing

Chronic diseases (CD), characterized by a prolonged disease period with persistent symptoms, are a leading cause of death worldwide. Among the most prominent CD are chronic respiratory diseases (CRD), diabetes, and chronic kidney diseases (CKD). Chronic diseases account for 70% of all health expenditures and are a significant health threat to the aging population as well as the very young (Wang et al., 2013). In resource-limited regions, the CD has a higher risk of resulting in the death of a patient. As the disease

progresses, patients frequently experience numerous acute health problems and complications, negatively impacting their overall quality of life (Drain et al., 2014).

A rapid diagnosis of CD is necessary so that treatment can be started as early as possible. Regular monitoring is also highly beneficial for understanding and managing an individual patient's condition as it progresses. However, CD diagnosis often requires expensive diagnostic procedures with long turn-around time. A patient needing a blood test must travel to a hospital to have a sample drawn. This sample will likely be sent to a centralized laboratory for analysis and take days before the patient obtains their test results. Current diagnostic procedures also struggle with high-costs, complicated assay procedures, low test speed, and the requirement of specialized training and equipment.

Point-of-care devices have become the subject of great interest in recent years as a potential solution to these limitations. A familiar example of a POC device is blood glucose meters which help diagnose and manage diabetes. Ideally, a should meet the ASSURED (affordable, sensitive, specific, user-friendly, rapid and robust, equipment-free and delivered) standard published by the World Health Organization (Drain et al., 2014). Thus far no POC test has fully satisfied the ASSURED criteria.

At present, the main limitation is that current POC devices suffer from reduced accuracy and remain prohibitively high for resource-limited regions. Thus, significant motivation exists to support the development of tools and technology for a rapid, reliable and cost-efficient POC test.

CHAPTER 3

DESIGN & FABRICATION

The design parameters for this thesis were as follows:

- 1) Simplify assembly of the microfluidic device by integrating interconnects.
- 2) Improve the user-friendliness of the device.
- 3) Maintain cost-effectiveness and ease of modification.

The first parameter was fulfilled by creating housing that both locks the device in place while also helping align the interconnects. The third parameter was achieved by using 3D printing and off-the-shelf parts to construct the housing. In this chapter, the design and fabrication of the physical platform are detailed. The creation of a LabVIEW program to control the fluidic component of the device and improve ease of operation is described in the next chapter.

3.1 Design

3.1.1 Housing

The first component was designed as a holder that would secure the chip. This was accomplished by modeling a rectangular plate and cutting a recessed groove into the surface for the chip to rest in. The groove was made with dimensions $76 \times 26 \times 2 \text{ mm}^3$. The length and width of the groove were made 1mm larger than the actual dimensions of the glass slides used to make the device. This is because the 3D printing process involves heating an extruded spool of plastic that is deposited onto a build surface. The plastic

material contracts as it cools, necessitating dimensions in the horizontal plane be larger to offset this effect.

Because the chip is assembled from two glass slides stacked on top of each other with an offset, a 1mm high “step” was added so that the overhanging portion of the top slide would have additional support (**Figure 3.1A**).

Next, it was necessary to accommodate the variation in the precise position of the electrode pads. One end of the chip was treated as a fixed position, while the other end would be a variable distance away. A sliding element was created to facilitate the movement of one set of probes along the length of the chip (see **Figure 3.3** below). Two grooves were cut into the plate, flanking the recess for the chip on either side (**Figure 3.1B**). For the stationary set of probes, an opening was cut into the step of the holder (**Figure 3.1C**), where the probes would be mounted. Finally, to enclose the entire system, a lip was added to the outer edge of the holder so that a top and bottom lid could snap shut around it (**Figure 3.1D**).

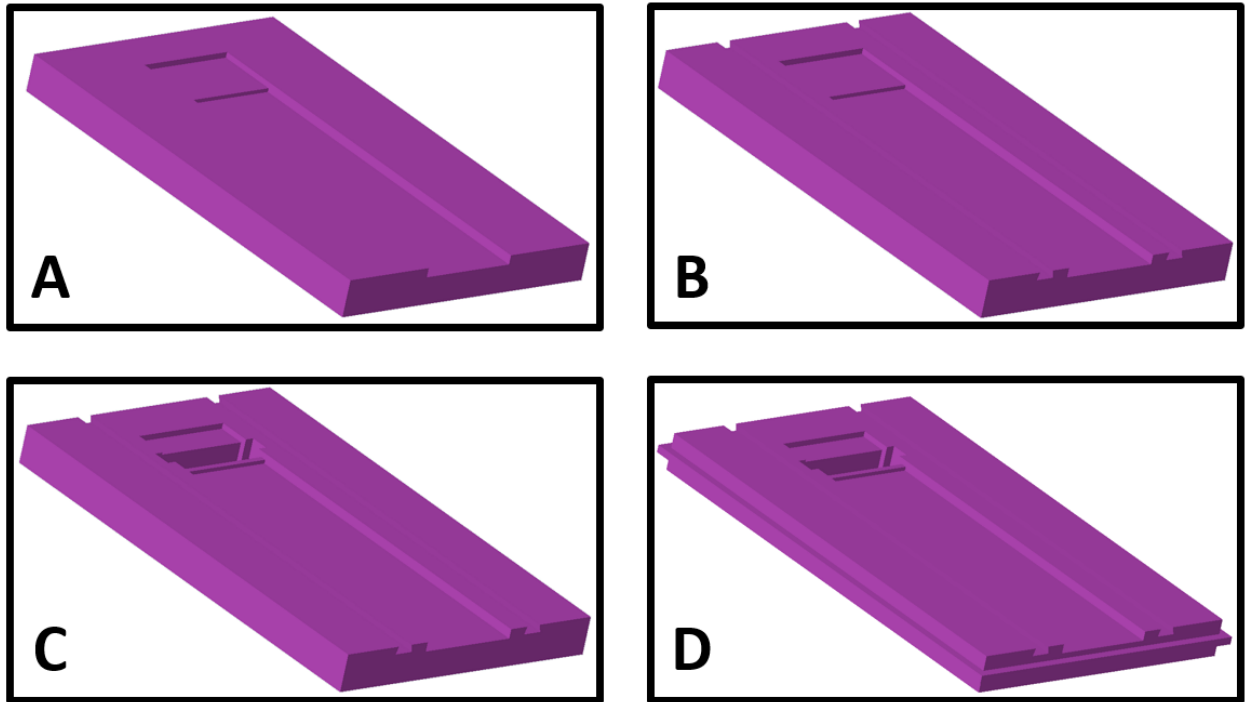


Figure 3.1 - Creo Parametric model of the housing at various stages of design:
 A – recessed groove for chip B – rails for slider bar C – opening for spring probes D – lip to join enclosure.

3.1.2 Spring Probes

The next challenge was to design an electrical interconnect between the electrode contact pads on the microfluidic chip and the EIS analyzer. The standard method is to solder a wire directly onto the pad and then connect the other end to the EIS. This has the advantage of being simple to implement and reliably bonding the wire to the chip. However, the need to solder adds to the fabrication time for assembling a functional microfluidic device. Furthermore, the connection is, from a practical standpoint, permanent and not easily removed or undone. While this is beneficial in making secure connections, it makes the process of disassembling chips for repurposing difficult and time-consuming.

An alternative way to connect to the pads would be to use some probe that could be attached securely and then removed when no longer requires. A study by Lee et al.

investigated by an optical microscope the effects of probing with a needle-like probe and ordinary alligator clips on a gold electrode (Lee et al., 2014). The optical microscope images in **Figure 3.2** show how the gold electrodes were damaged or deformed by probing. The flat gold electrode before probing (**Figure 3.2A**) was deformed by scratches (**Figure 3.2B, C**). The mechanical contact of needle-like probes left short scratches from sliding against the surface of the gold electrode. Manual clipping of an alligator clip left more intense scratches on the gold electrode as the manipulation was subject to shaking and movement.

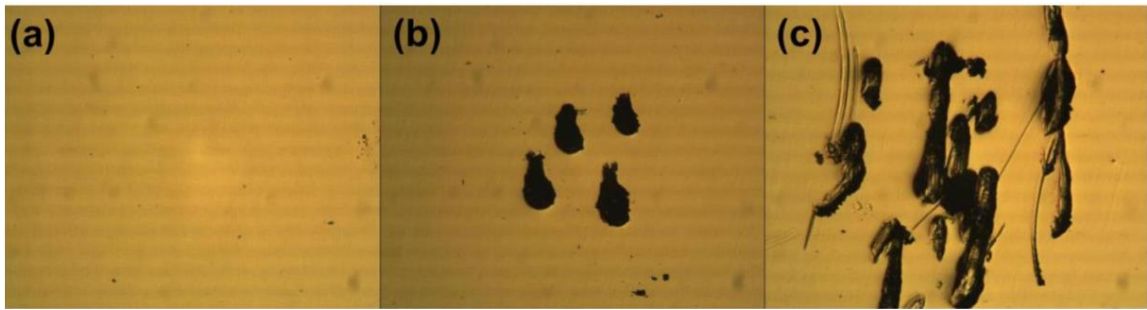


Figure 3.2 A - An optical microscopic image of flat gold electrode B - Optical microscope image of a flat gold electrode after five successive measurements using a needle-like probe C - Optical microscope image of a flat gold electrode after five consecutive measurements using an alligator clip.

Source: Lee, M.-K., Lee, T. J., Choi, H. W., Shin, S. J., Park, J. Y., & Lee, S. J. (2014). A universal system for reliable probing of electrochemical lab-on-a-chip devices. *Sensors (Basel, Switzerland)*, 14(1), 944-956. doi:10.3390/s140100944.

Since scratches are caused by mechanical abrasion on metal layers by shear forces, it was desirable to find a probing apparatus that would use minimal shear force direction (Temiz, Lovchik, Kaigala, & Delamarche, 2015). This could be realized by approaching and pressing the pad from a purely vertical. Spring probes proved to be ideal for this application since they provide the moderate contact pressure needed to reduce or eliminate

unstable contacting and their movement in the vertical axis will prevent deformation of the gold electrode.

One set of electrode pads would be at a fixed position while the other would be at a variable distance away. For the fixed pads, recessed openings were incorporated into the holder. The openings were positioned so that they would align with the pads as the chip is inserted. The depth of these recesses was precisely adjusted so that spring-probes were only partially retracted. Thus, when a chip was inserted, pads would align with and press down on the probes. The resistive force of the springs would then push back against the pads to form a reliable connection.

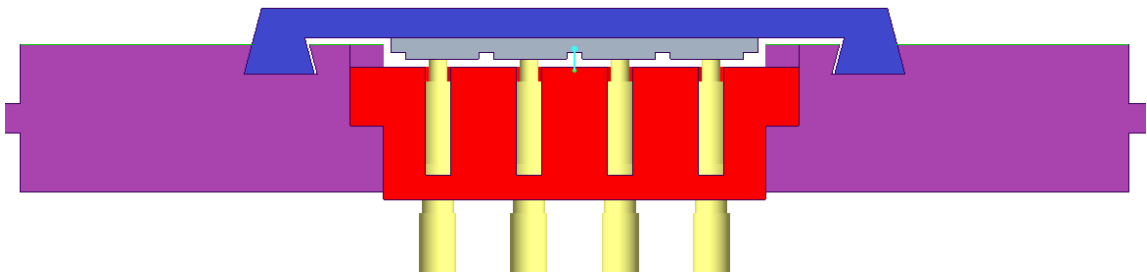


Figure 3.3 Cross-section of the holder. The probes (yellow) are only partially retracted and automatically align with the chip (gray) when it is placed in the holder (purple). The slider bar (blue) prevents the chip from coming loose.

For the pads at the variable position, the spring probes were firmly mounted in a slider that aligns the probes and positions them above the pads. These probes were mounted at right angles to eliminate shear force.

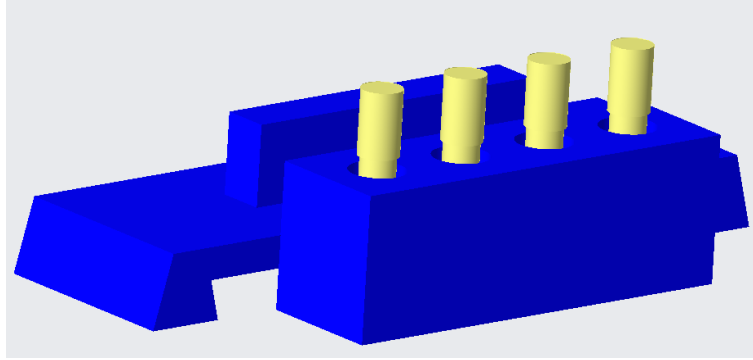


Figure 3.4 Creo Parametric model of the slider (blue) with probes (yellow) inserted.

The back end of the spring-probes would be soldered to wires that led to a measuring instrument. For this thesis, the tool was an Agilent 4294A impedance analyzer.

3.1.3 Enclosure

A top and bottom enclosure were designed to protect the device and the electrical wiring. The top enclosure had two openings to allow fluid tubing to reach the device while the bottom enclosure had openings for the wires to connect to instrumentation.

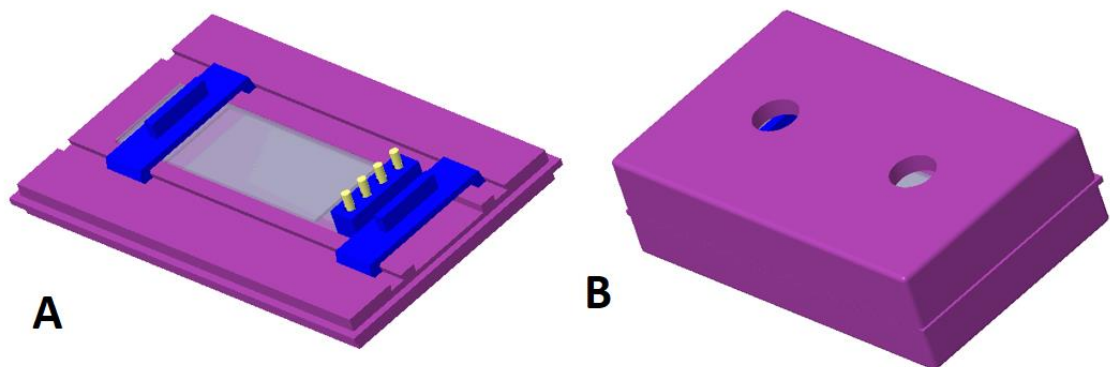


Figure 3.5 A - Creo Parametric model of the chip (gray) inserted into the holder (purple) and locked into position by sliders (blue). B – Assembled housing with top and bottom enclosure.

3.2 Fabrication

The housing, sliders and enclosure were all fabricated using an Ultimaker series 3 3D printer. This model of printer has a layer resolution of up to 20 μm , making it well-suited for producing the small, precisely fit components required.

The material used for all printing was polylactic acid (PLA) plastic which was selected for ease of printing and lower cost compared to other plastics such as polyethylene terephthalate (PETG). It has the notable drawback of having a lower maximum service temperature and being more brittle than other plastics. However, as this particular platform is still intended for laboratory use, these were considered to be acceptable.

The probes are in-line, spring-loaded contacts (ED1055-ND) made by Mill-Max Manufacturing and purchased through Digi-Key. The probe is made of beryllium copper alloy with gold finish measuring 0.51 μm thick. This particular model was chosen because the bottom has a cup-shaped depression specifically designed to facilitate the soldering of wires.



Figure 3.6 ED1055-ND spring probe. Image taken from <https://www.digikey.com/product-detail/en/mill-max-manufacturing-corp/0854-0-15-20-82-14-11-0/ED1055-ND/2732560> in December 2019.

Wires were soldered to the spring probes and the probes then inserted into the recesses in the 3D printed holder and slider. An epoxy adhesive was applied to the recesses to securely fix the probes in a vertical orientation to prevent the shear and scratching of the

electrode pads. After that, the assembly was extraordinarily straightforward and required little more than snapping the various components together. Since the parts were 3D printed to precise specifications, the components fit securely without the need for additional fasteners or adhesives.

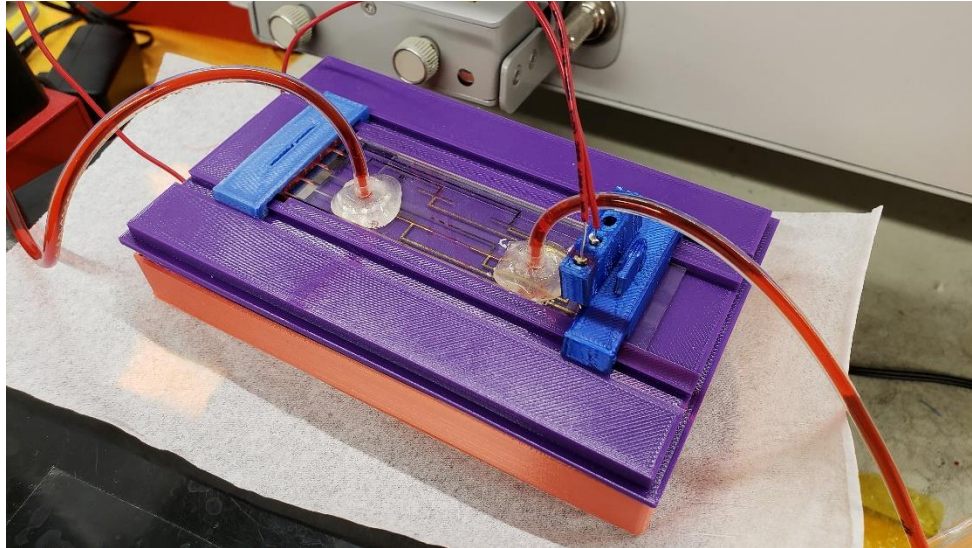


Figure 3.7 Assembled housing with chip (top enclosure removed for visibility).

Excluding miscellaneous costs such as shipping fees, adhesives, and tools the total cost of fabricating and assembling the housing was approximately \$50. In contrast, commercially available chip holders such as the Micronit Fluidic Connect Pro cost over \$1,200. Additionally, while the particular design presented here is intended to work in tandem with chips currently utilized by the New Jersey Institute of Technology's Opto and Microfluidics Laboratory, the design could easily be adapted to a variety of chip designs and configurations. The CAD models used for the 3D printing could be open-sourced and anyone needing such an interface could customize the design by adjusting the parameters of the original file.

CHAPTER 4

LabVIEW

This chapter begins with an introduction to the features of the LabVIEW software and continues with an overview of the program created to control the syringe pump for this application.

4.1 Features of LabVIEW

LabVIEW (Laboratory Virtual Instrument Engineering Workbench), is a programming environment developed by National Instruments. It accommodates data acquisition, instrument control, data processing and data presentation. LabVIEW differs from traditional high-level languages such as C, Pascal or Basic in that it uses a graphical programming language (sometimes called “G” language).

LabVIEW programs are called “virtual instruments” (VIs). Each VI has three components: (1) a front panel, (2) a back panel, and (3) a connector pane.

The front panel is a user interface that is constructed using controls and indicators. Controls are inputs that allow a user to pass information into a VI. Indicators are outputs and display results produced based on the inputs given to the VI. The back panel is a block diagram that contains the graphical source code. All objects placed in the front panel will appear on the back panel as terminals.

The back panel also contains structures and functions that perform operations on data received from controls and output data to indicators. Controls, indicators, structures, and functions are represented as nodes that can be connected using wires that represent the

flow of data through the VI. For example, two controls accepting numeric inputs and an indicator can be wired to the “addition function”, and the indicator will display the sum of the two controls.

The connector pane is used to represent a VI in the block diagram of other VIs that call it, allowing for a VI to act as a subroutine (subVI) in a more extensive program.

The graphical nature of the G language makes LabVIEW more accessible to nonprogrammers since they can build programs by dragging and dropping virtual representations of familiar lab equipment, controls or indicators (e.g. thermometers, toggle switches, dials). However, while it is straightforward to create small applications, more large-scale code can become confusing without an understanding of the unique syntax of the graphical language.

4.2 Front Panel

This section covers the front panel and the essential controls and indicators presented to the user as part of the interface.



Figure 4.1 Front panel of the Pump Control VI.

4.2.1 Serial Communication

These three controls input information necessary for serial communication between a computer and the NE-1000 syringe pump.

The **baud rate** describes the rate at which information is transferred to a communication channel. In **Figure 4.2** below it can be seen that the baud rate is set to 19200, meaning the port is transferring 19200 bits per second. This baud rate was obtained from the operating manual for the NE-1000 and should not be changed unless a different pump is used.

The **pump number** is an index value that indicates where a pump is in a network. The NE-1000 pump can be networked together with other NE-1000s, all controlled by the same computer. However, this must be done by connecting the pumps serially, one into the next in a daisy chain. Thus, the pump number index is necessary to ensure inputs are sent to the right pump in the network.

The **VISA resource name** identifies the I/O port through which the LabVIEW program is communicating with an external device. This name will change depending on how the device is connected to the computer.

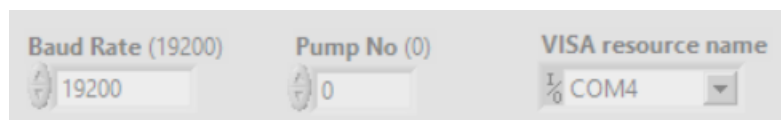


Figure 4.2 Serial communication controls.

4.2.2 Pumping Parameters

These controls input the parameters that determine the behavior of the pump.

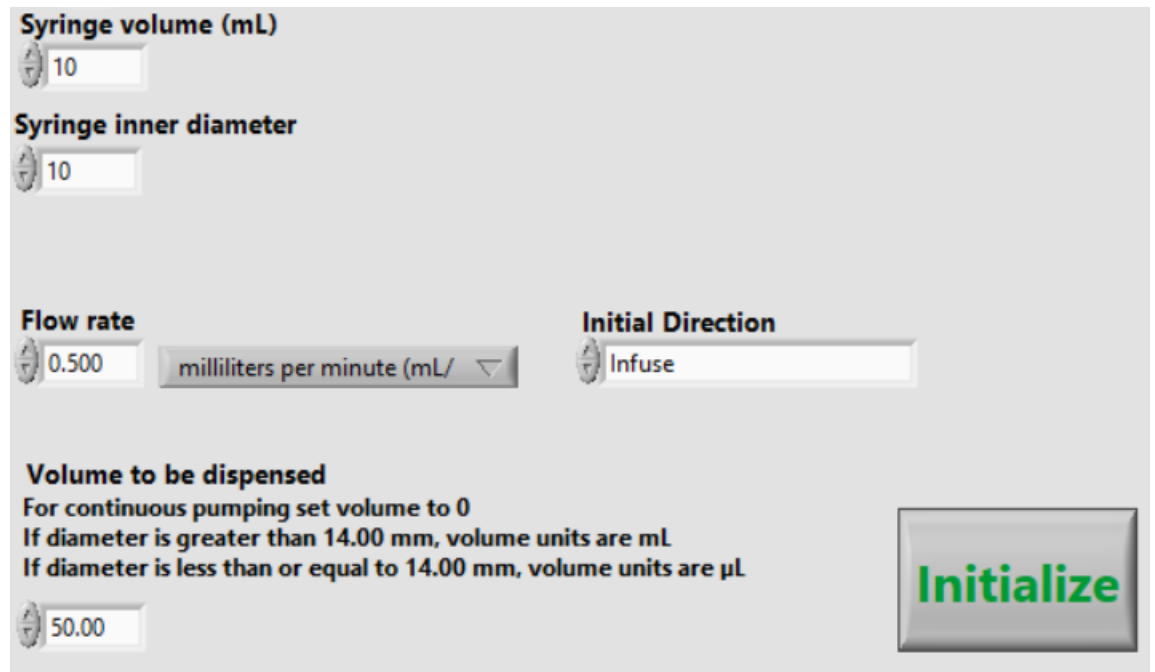
Syringe volume and **Syringe Inner Diameter** are the dimensions of the syringe connected to the pump.

Flow rate is the volume of fluid being pumped out in a given interval of time. There are four possible units for this input: μL per minute, μL per hour, mL per minute and mL per hour. This is reflective of the four flow rate units built into the NE-1000.

Initial direction controls whether the syringe will pump fluid out (infuse) or will draw fluid in (withdraw) when the program starts to run.

Volume to be dispensed is the volume of fluid to be pumped out. Note that if this is set to 0, the pump will run continuously at the specified flow rate until stopped. Also note that the units of this input change from mL to μL based on the diameter of the syringe. This was determined from the examination of maximum flow rates for specific diameters as listed on the NE-1000 user manual.

The **Initialize** button will upload the input parameters to the syringe pump. The pump will then standby waiting for a “**Run**” command.



The image shows a software interface for configuring a syringe pump. It features several input fields and a large button. The fields are: 'Syringe volume (mL)' with a value of 10; 'Syringe inner diameter' with a value of 10; 'Flow rate' with a value of 0.500 and a dropdown menu set to 'milliliters per minute (mL/'; 'Initial Direction' with a value of 'Infuse'; and 'Volume to be dispensed' with a value of 50.00. Below the 'Volume to be dispensed' field, there is explanatory text: 'For continuous pumping set volume to 0', 'If diameter is greater than 14.00 mm, volume units are mL', and 'If diameter is less than or equal to 14.00 mm, volume units are μL '. A large green 'Initialize' button is located in the bottom right corner.

Figure 4.3 Pumping parameter controls.

4.2.3 Operating Controls

These controls are used to operate the pump once the parameters are uploaded.

The **Run** button will signal the pump to start pumping. This will continue until the input **Volume to be dispensed** is reached or, in the case of a flow rate of 0, until the **Stop** button is pressed.

The **Stop** button will halt the pumping process and terminate the program immediately

The **Pause** button will halt the pumping process but will not end the program.

The **Reverse** button will switch the pumping direction to the opposite of what it is currently (i.e. infuse will become withdraw and vice versa).



Figure 4.4 Operating controls.

4.2.4 Indicators

These indicators provide information about the pump while the pumping is in progress.

The **Status** indicator consists of a series of LEDs that show what the pump is currently doing, whether Stopped, Infusing/Withdrawing, or Paused.

The **Speed** indicator includes both a numerical and graphical indicator of how fast the pump is moving to help the user make sure the pump is working within safe operating limits.

The **Volume Dispensed** indicator shows the volume of fluid dispensed or withdrawn by the pump thus far in real-time.

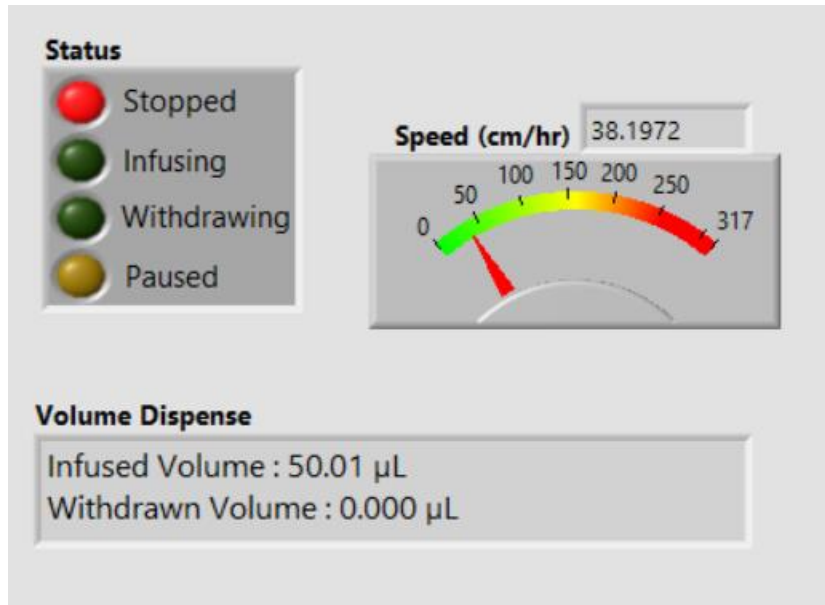


Figure 4.5 Indicators.

4.3 Back Panel

This section will examine the back panel of the VI and work through the block diagram of the entire program. Please note that for organization, the VI is discussed in “modules” but these are not necessarily representative of actual structures in the VI.

Please also note that throughout the block diagrams there are blue squares that represent subVIs. These subVIs were downloaded from the National Instruments website and perform fundamental tasks (e.g. check if the pump is turned on, check if the pump is running) and act as building blocks for more extensive operations.

4.3.5 Initialization Module

This module reads in the **Serial communication** inputs (see 4.2.1) and initializes the pump. It does so by first establishing communication, checking for firmware compatibility, checking for sufficient power, and then clearing the memory of the previous volume dispensed.

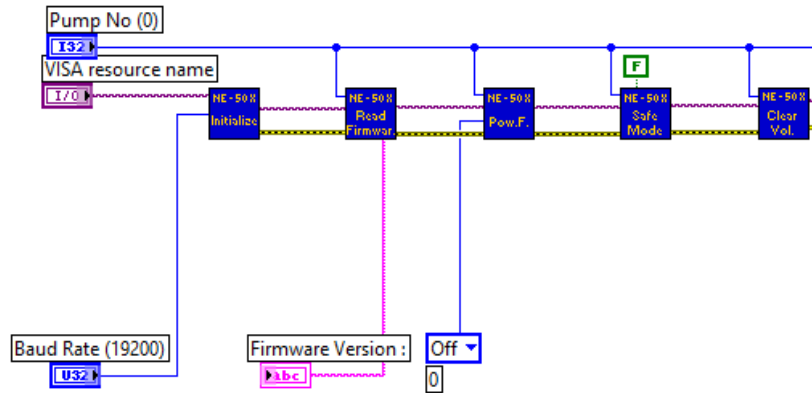


Figure 4.6 Block diagram of the initialization module.

Note the blue wire that runs along the top of the diagram. This passes the information about the **pump number** (see 4.2.1) to all the subVIs and runs the length of the block diagram. Likewise, the purple wire passes on information about the port being used for serial communication must, therefore, run throughout the VI to connect all subVIs that send or receive data from the pump.

Additionally, the yellow-and-black wire is dedicated to error handling. If an error occurs, usually the result of missing or erroneous information, this wire will cascade through the VI and terminate the program by presenting an error message as well as information on the cause.

4.2.5 Pumping Parameter Module

This module reads in the **Pumping parameters** input (see 4.2.2) and sends the information to the pump. Note that in the lower-left of **Figure 4.6** is a true-or-false case structure that switches between mL and μ L units for the **Volume to be dispensed** if the input **Syringe inner diameter** is greater than 14mm.

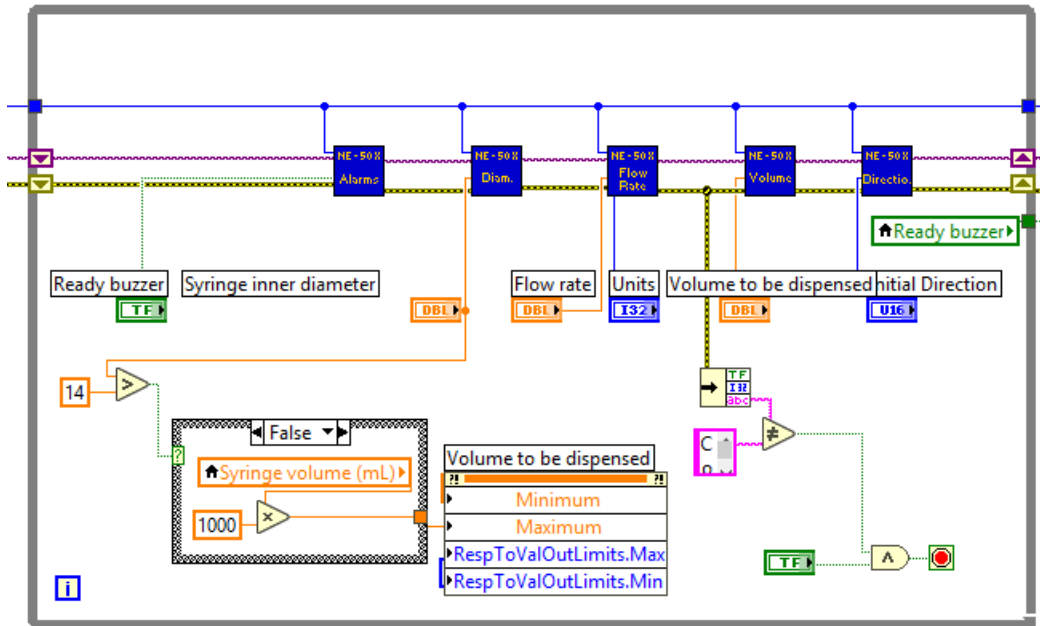


Figure 4.7 Block diagram of the pumping parameter module.

This module is enclosed in a while-loop structure (the gray box in **Figure 4.6**), meaning the program will continue reading in **Pumping parameters** and sending them through to the pump. In other words, changing any of these inputs will update the parameters displayed on the syringe pump in real-time. The while-loop terminates when the user presses the **Initialize** button, which has a corresponding Boolean terminal that appears as a green “TF” in the lower-right of **Figure 4.6**. Once the button has been pressed, the loop ends, the parameters can no longer be changed freely, and the next module executes.

4.2.6 Operations Module

Because of the complexity of this module, the block diagram in **Figure 4.7** has been marked with lettered red boxes to point out important areas. An unmarked block diagram is included in **Appendix A** as **Figure A.3** and **Figure A.4**.

Once the data from the previous module is received, the following sequence occurs:

A – The **Status** of the pump is queried. The **Status** is returned as an array of Boolean values for the following conditions: Stopped, Infusing, Withdrawing, Paused, Pause phase, Trigger wait.

B – The cells within the **Status** array that contain Boolean values for Infusing and Withdrawing are checked. These Boolean values are passed through a logical “or” operator that returns false if both input values are false and return true otherwise. Therefore, if the pump is neither infusing nor withdrawing, then it must currently be in a “stopped” state and passes on a false.

C – Since the pump is currently stopped, check to see if the user has pressed the **Run** button. If the button has been pressed, the corresponding Boolean terminal will switch to true.

D – If the **Run** button is not down, the corresponding Boolean terminal is set to false, and nothing occurs. When a true signal is received from the **Run** button, the pump starts.

E – If the **Pause** button is not down, the corresponding Boolean terminal is set to false, and nothing occurs. If the **Pause** button is pressed down, the corresponding Boolean terminal is set to true and the pump is stopped.

F – Checks the **Flow rate** parameter. If the rate has changed, the new rate is updated on the pump.

G – If the **Reverse** button is not down, the corresponding Boolean terminal is set to false, and nothing occurs. If the **Reverse** button is pressed down, the corresponding Boolean terminal is set to true and the pump switches direction.

H – The various indicators are updated before the whole module repeats itself in a while-loop. The program will continually check for user input and respond accordingly, pump out fluid, update the indicators and so forth until the loop is terminated.

I – The while-loop enclosing this module terminates when either the **Volume to be dispensed** is entirely dispensed or when the user presses the **Stop** button.

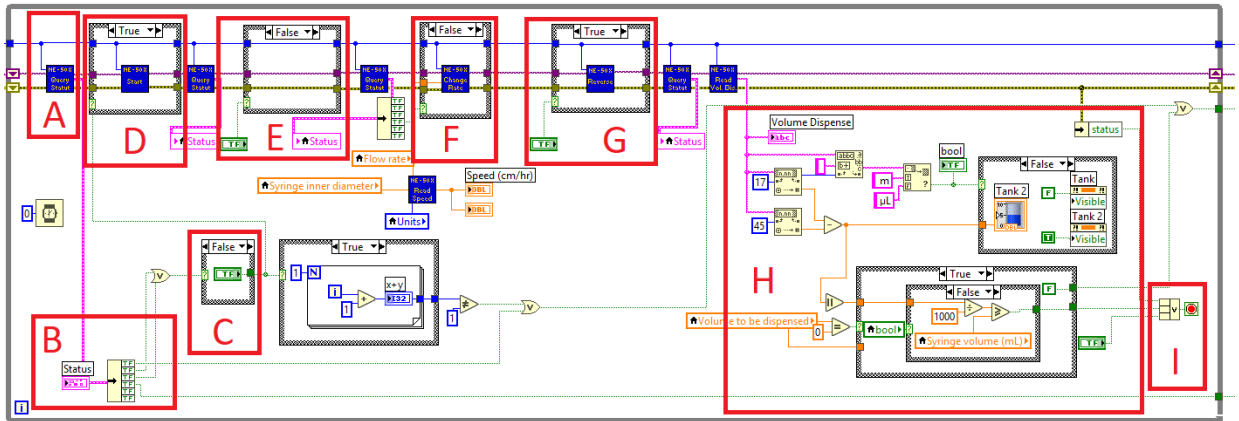


Figure 4.8 Marked block diagram of the operations module.

4.2.7 Termination Module

This module performs various upkeep tasks to prepare the pump to be shut down or to start a new pumping sequence. First, the status of the pump is checked a final time, then the pump memory is cleared, and the I/O port is closed.

Note that this is where the yellow-and-black error wire terminates. If there is no error and the pumping has completed successfully, a message is displayed to the user indicating as such (see **Figure 4.8A** below). Alternatively, if an error has occurred at any point in the program, it propagates down the yellow-and-black wire to here, where it prompts the program to display an error message for the user.

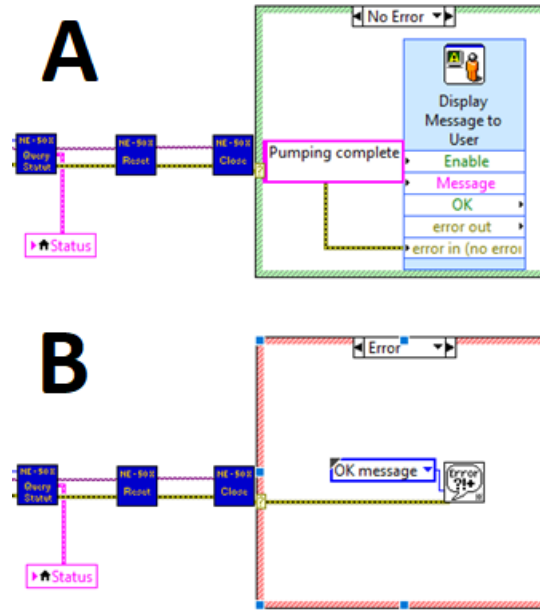


Figure 4.9 A - Block diagram of the termination module after completion of a successful pumping sequence. B – Block diagram of the termination module after an error occurs.

CHAPTER 5

MATERIALS AND METHODS

5.1 Materials

Experiments were conducted to validate the efficacy of the design. The objective of these experiments was both to confirm that the design would not leak and that the electrical connections provided by the spring probes yielded a sensitivity that was comparable to the standard method of directly soldering wires to the electrode contact pads. The following materials were used in the course of these experiments.

5.1.1 Glass Slides

Standard glass slides (1304G) with ground edges, 90° corners, and dimensions of $25 \times 75 \times 1 \text{ mm}^3$ are obtained from Globe Scientific Inc. The fabrication of the microelectrodes on the glass slides is performed in the Nanofabrication facility at CUNY Advanced Science Research Center.

5.1.2 Adhesive Tape

A double-sided polyester tape (90445) is obtained from Adhesive Research Inc. This tape is coated on both sides with a medical-grade, pressure-sensitive SR-26 silicone adhesive. The sides are protected by a layer of polyester release liner covering both sides.



Figure 5.1 Cross-section of layers of adhesive tape.

Source: <https://www.adhesivesresearch.com/wp-content/uploads/2013/10/90445-Data-Sheet.pdf>.

5.1.3 Deionized Water

The deionized (DI) water used in all the experiments was produced by a Milli-Q Direct 8 Water Purification System machine obtained from Millipore Sigma. The conductivity measured as $7.6 \mu\text{S}/\text{cm W}$.



Figure 5.2 Milli-Q Direct 8 system used to produce DI water.

5.1.4 Food Colorant

The food colorant used as a food-grade colorant obtained from McCormick & Company which are non-toxic and degradable dyes. The red food colorant was diluted by adding 5 drops to 10ml of distilled water.



Figure 5.3 Red food colorant diluted in DI water.

5.1.5 Fluorescein

Fluorescein was obtained from Acros Organics and was used for the fluorescent microscopy experiment. Fluorescein is a commonly used fluorophore for such applications. It has a molecular formula of $C_{20}H_{12}O_5$, a molecular weight of 332.31 g/mol and excitation at 494 nm with peak emission at 521 nm. It was diluted to molarity of 10 $\mu\text{mol/mL}$ in DI water and stored in dark, refrigerated conditions until use.

5.1.6 Potassium Chloride

The potassium chloride (KCl), ACS grade was obtained from British Drug Houses (BDH) and diluted with DI water to reach the required KCl concentrations from 1M to 1 μM .

5.1.7 Probe and Target DNA

Probe-DNA and target-DNA oligo with the sequence 5'-/-5AmMC6/CGTCCAAGCGGGCTGACTCATCAAG-3' and 5'-CTTGATGAGTCAGCCCGCTT GGACG-3', respectively are obtained from Integrated DNA Technologies (IDT).

5.1.8 Functionalization Reagents

A10807 1-(3-dimethylaminopropyl)-3-ethyl carbodiimide hydrochloride (EDAC) and A10312 N-Hydroxysuccinimide (NHS) are purchased from Alfa Aesar at 98%+ purity. 2-(N-Morpholino) ethanesulfonic acid hydrate (MES) is acquired from Sigma-Aldrich with 99.5%+ purity.

5.1.9 Phosphate Buffered Saline

Phosphate buffered saline (PBS) tablets are purchased from VWR and dissolved in 100 mL of water. The pH of the resulting solution was measured to be 7.4. The 1 X solution was then diluted to produce a 0.1 X and 0.01 X solution.

5.1.10 Carbon Nanotubes

The carboxylic acid-functionalized short single-walled carbon nanotube (C-SWCNT, 98%+) are obtained from US Research Nanomaterials Inc.

5.2 Apparatus

5.2.1 Cricut Explore®

The Cricut Explore® device was used to cut the microfluidic channel into the tape. The design was created in AutoCAD and transferred to the Cricut software. A thin section of adhesive tape was cut from the roll and aligned to the cutting mat. The mat is loaded into the Cricut machine which uses a fine point blade to cut a channel to the desired design. The Cricut was set to use the cutting parameters for vinyl to ensure that the cuts would be deep enough to penetrate the outer layer of the liner as well as the actual adhesive underneath.

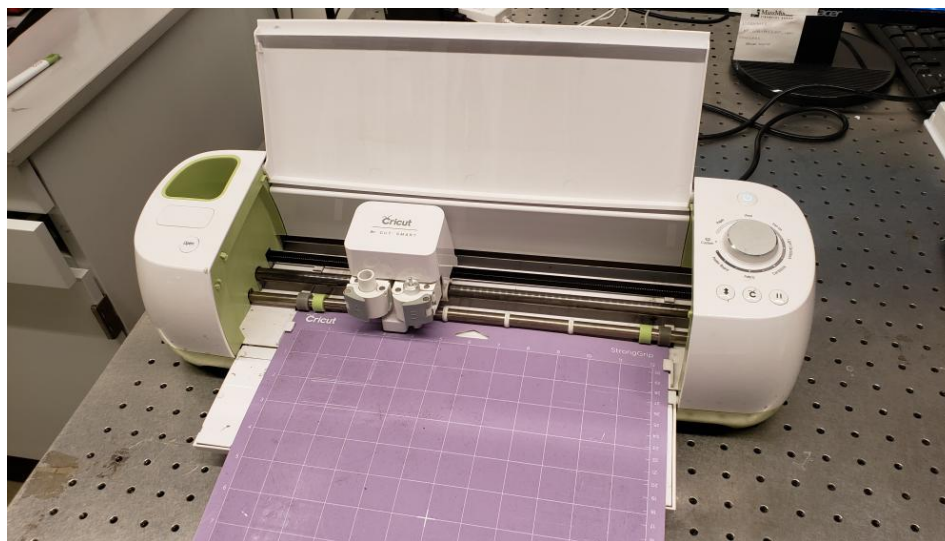


Figure 5.4 Cricut Explore® cutting machine with a cutting mat inserted.

5.2.2 NE-1000 Syringe Pump

The New Era Systems NE-1000 series Programmable Syringe Pump was used for all of the following experiments. The pump provided the pressure to drive the flow of fluid through the device while also maintaining the flow rate at the desired level. A 3ml BD syringe with an inner diameter of 8.66mm was used to deliver the various fluids being pumped. The syringe was clamped into the syringe pump and then connected to the microfluidic chip using Tygon® tubing manufactured by Saint Gobain. Fluid ports were used to provide tight, leak-proof connections between the tubing and attached components. The parameters of flow rate, volume dispensed, and syringe dimensions were input using the interface created in the LabVIEW program (described in **Chapter 4**) but were also confirmed on the pump's built-in display.



Figure 5.5 NE-1000 Syringe Pump.

5.2.3 Drill Press

A Model 38119 Central Machinery® 5-speed drill press was used to drill holes into the top glass slides to form the inlet and outlet for the microfluidic channel. The 1mm diameter drill bit was used to drill both holes. The position of the holes depended on the position of the ends of the channel, leading to some variation in the precise location of the inlet and outlet.

5.2.4 Fluorescence Microscope

An Olympus BX-51 fluorescence microscope from Spectra Services was used to view the fluorescent images. The images were captured with an attached Hamamatsu C11440 digital camera.



Figure 5.6 Olympus microscope with attached Hamamatsu digital camera.

The Olympus fluorescence microscope produces ultraviolet (UV) light and directs it into the interference filter block (see **Figure 5.7** below) where it strikes a dichroic mirror. A dichroic mirror reflects one range of wavelengths and allows another range to pass through. The ultraviolet light is reflected and directed onto the specimen. This light excites fluorescence within molecules in the sample. For this experiment, the molecules in question are fluorescein dye dissolved in water. The objective lens then collects the fluorescent-wavelength light produced. This fluorescent light passes back through the dichroic mirror and a barrier filter eliminates any wavelengths other than the fluorescent wavelengths to resolve the image.

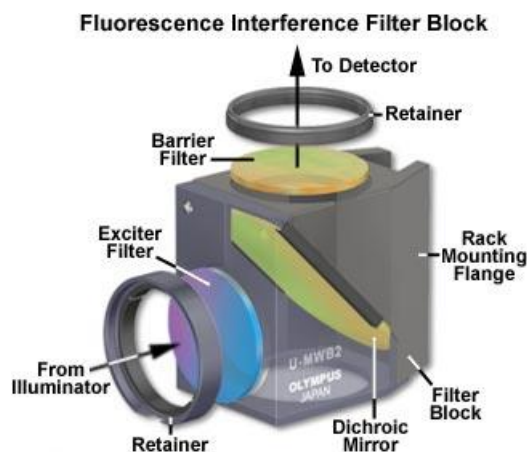


Figure 5.7 Fluorescence filter block of Olympus microscope.

Source: <https://www.olympus-lifescience.com/en/microscope-resource/primer/techniques/fluorescence/filters/>.

5.3 Device Fabrication

The microchannel is constructed out of AR90445 double-sided tape. The microfluidic channel is cut using the Cricut Explore®. The dimensions of the channel are 48mm (L) × 500µm (W) × 142µm (H). The completed device consists of a microchannel cut into the double-sided tape sandwiched between the top and bottom patterned microelectrode. Inlet and outlet holes for the fluid flow are drilled using the 1mm diamond drill bit. The adhesive is used to secure the top and bottom microelectrode glass slides.

Two chips were assembled for these experiments. The first had an empty (unpacked) channel while the second one was packed with C-SWCNT functionalized with probe DNA.

30 mg of the C-SWCNT is vortexed in the 0.1M MES buffer solution and centrifuged in a 1.7 ml Eppendorf at 6000 rpm (GeneMate Minifuge) three times. During the wash, the suspension is regularly replaced with a fresh MES buffer. The supernatant is then extracted and activated via the EDC-NHS coupling reaction with probe-DNA oligo in

1× PBS solvent overnight. The DNA-functionalized C-SWCNT is then washed in 1× PBS and preserved in the refrigerator until use.

5.4 Food Colorant Run Protocol

The food colorant is diluted in DI water and vortexed. An unpacked chip is placed into the housing and connected to the syringe pump. The LabVIEW pumping program is set to wash the device with DI water for 1 hour. After the wash procedure, a syringe loaded with 2ml of colorant solution is placed in the pump. The LabVIEW pumping program is then set to run at a rate of 1 μ l/min for 2 hours. After 2 hours, photographs of the device and the microfluidic channel were taken.

5.5 Fluorescence Microscopy Protocol

The fluorescein is diluted in DI water and vortexed. An unpacked chip is placed into the housing and connected to the syringe pump. The LabVIEW pumping program is set to wash the device with DI water for 1 hour. After the wash procedure, a syringe loaded with 2ml of fluorescein solution is placed in the pump. The syringe, pump, and chip were covered with aluminum foil to prevent degradation of the dye during the pumping processes. The LabVIEW pumping program is set to run at a rate of 1 μ l/min for 2 hours. After 2 hours, photographs of the device and the microfluidic channel were taken using the FITC filter on the fluorescence microscope.

5.6 Flow Rate Validation Protocol

The LabVIEW program uses the instrumentation of the NE-1000 syringe pump to track flow rate. Thus, it is necessary to validate that the flow rate registered by the pump is indeed accurate. To test this, a syringe filled with DI water was loaded into the pump and set to dispense continuously at a specified flow rate. The water was allowed to flow through the device and to the end of the tubing connected to the device's fluid outlet in order to minimize the effect of dead volume. After the flow had stabilized, the tubing was positioned to dispense water into an Eppendorf tube and allowed to run for a set period of time. When the time had elapsed, the pump was stopped and the volume of water in the tube was measured. Measurements were done by taking the mass of the tube containing water and subtracting the mass of the tube itself to yield the mass of the water inside. Using the density of water, 1 g/mL or 0.001g/ μ L, it was possible to calculate the volume of water. The volume of water dispensed was then divided by the time elapsed to yield an actual flow rate which was then compared to the flow rate registered by the pump's built-in instrumentation. This was performed using four different flow rates and each flow rate was tested four times, as outlined in **Table 5.1** below:

Table 5.1 Parameters of Flow Rate Validation Experiments

Condition	Number of runs	Flow rate (μ L/min)	Time (min)
1	4	0.5	50
2	4	1.0	30
3	4	5.0	10
4	4	10.0	5

5.7 KCl Run Protocol

Note that for the subsequent experiments, the following terminology is used to describe the various electrode configurations that can be implemented on the ESSENCE microfluidic device. These terms are taken from the designations used by Cheng et al. in their article.

Different Electrode Configurations

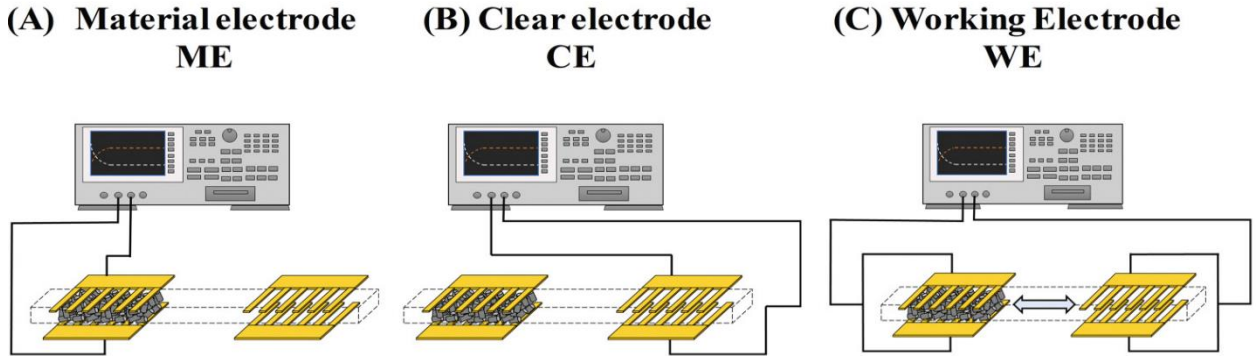


Figure 5.8 Electrode configurations for the ESSENCE microfluidic device.

Source: Cheng, Y. H., Moura, P. A. R., Zhenglong, L., Feng, L., Arokiam, S., Yang, J., . . . Basuray, S. (2019). Effect of electrode configuration on the sensitivity of nucleic acid detection in a non-planar, flow-through, porous interdigitated electrode. *Biomicrofluidics*, 13(6), 064118. doi:10.1063/1.5126452

Table 5.2 Description of Electrode Configurations

Designation	Description
ME – “Material electrode”	The EIS signal is taken from the set of electrodes packed with transducer material
CE – “Clear electrode”	The EIS signal is taken from the set of electrodes that do not have transducer material.
WE – “Working electrode”	The first set of electrodes with packing is shorted together to form the “working” electrode and the second set is shorted to create a “counter” electrode. The EIS signal is taken between the working and counter electrodes.

The KCl is diluted with DI water to get the required KCl concentrations from 1M to 10 μ M. An unpacked device is inserted into the holder and the electrode pads aligned

with the spring probes. The wires from the probes are connected to the Agilent 4294A impedance analyzer for EIS readings in the CE configuration.

The LabVIEW pumping program is set to wash the device with DI water for 1 hour. After the wash procedure is complete, a syringe of the KCl solution is placed in the pump and flows through the device at a rate of 1 $\mu\text{l}/\text{min}$ for 1 hour. The EIS signal for a given KCl concentration is then taken using the Agilent impedance analyzer.

5.8 Target DNA Run Protocol

A target-DNA oligo solution of 10 nM was obtained by diluting with 1 \times PBS. The DNA-functionalized C-SWCNT packed device is inserted into the holder, and the electrode pads aligned to the spring probes. The wires from the probes are connected to the Agilent 4294A impedance analyzer for EIS readings in the ME and WE configuration.

The device is first washed with 1 \times PBS solution at a flow rate of 1 $\mu\text{l}/\text{min}$ for 2 hours or until the EIS signal from the device stabilizes. The stabilization is considered to occur when there is no change between two EIS measurements that are taken 5 minutes apart. This stabilized EIS signal captured and considered to be the baseline measurement.

After stabilization, the target-DNA oligo solution is passed through the system at 1 $\mu\text{l}/\text{min}$ for 2 hours. Following the target-DNA oligo passage, the solution is switched back to 1 \times PBS solution as a wash at a flow rate of 1 $\mu\text{l}/\text{min}$ for 3 hours and 30 min to remove any unspecific bound target-DNA in the device. This difference between the EIS signal from the pre- and post-PBS wash is interpreted as the target-DNA oligo capture signal.

5.9 PBS Experimental Protocol

Two pumps, designated A and B, are prepared with separate syringes. Pump A is first connected to the device and runs for 20 minutes. After the 20-minute interval has elapsed, Pump B is connected and runs for 20 minutes. The pumps are alternated so that Pump A runs 5 times, and Pump B runs 5 times. EIS data is recorded every 5 minutes for all three runs in the CE configuration. The various parameters of each run are listed in the table below:

Table 5.3 Parameters of PBS Experiments

Run	Pump	PBS Concentration	Flow rate ($\mu\text{l}/\text{min}$)
1	A	0.001 X	10
	B	1 X	10
2	A	0.01 X	5
	B	0.01 X	5
3	A	0.01 X	1
	B	0.01 X	5

Run 1 varies the concentration of PBS between Pumps A and B. It is expected that while Pump A runs, the impedance measured will be significantly higher as the lower concentration of solute will reduce conductivity. Conversely, while Pump B runs, the impedance should be low as the higher concentration of solute improves conductivity. This run intends to demonstrate that the system changes in response to the change in impedance.

Run 2 maintains identical concentration and flow rate between Pumps A and B. Thus, it is expected that the impedances will very closely resemble one another.

Run 3 varies the flow rate between Pumps A and B. However, since the concentration of PBS remains the same, it is expected that the impedance will remain approximately the same when Pump A is running as when Pump B is running. This run intends to demonstrate the system remains stable even when flow rates are changed.

CHAPTER 6

RESULTS

6.1 Food Colorant Run

Visual inspection of the device after the passage of food colorant revealed no leaks. The red color is confined to the channel and has sharp, well-defined edges.

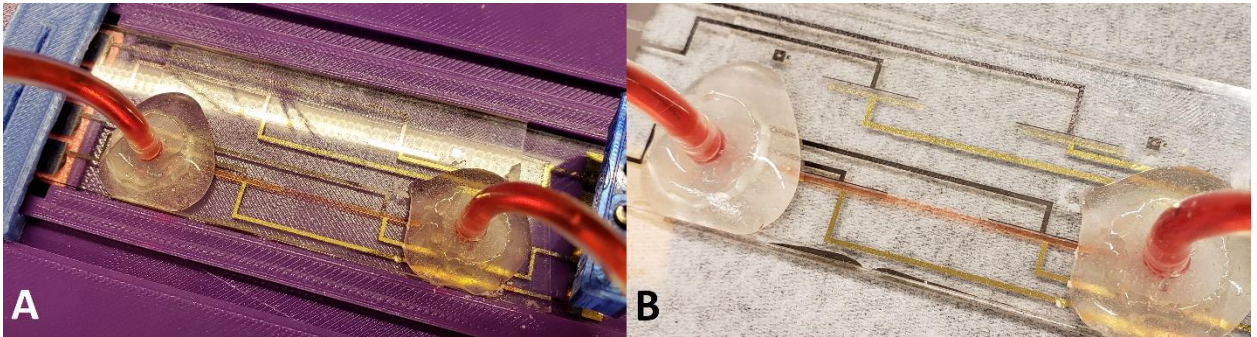


Figure 6.1 A – Photograph of the unpacked chip after food colorant run within the housing. B – Photograph of the unpacked chip after food colorant run on a paper towel for contrast.

6.2 Fluorescence Microscopy

The images in **Figures 6.2A** through **6.2D** show the results of the fluorescence microscopy. Visible in each image is the channel which appears brighter than the surrounding areas because of the fluorescein dye flowing through the channel. In **Figures 6.2A** and **6.2D**, the interdigitated electrodes are also visible. Since the bright regions are almost all confined to the channel, it appears there are no leaks.

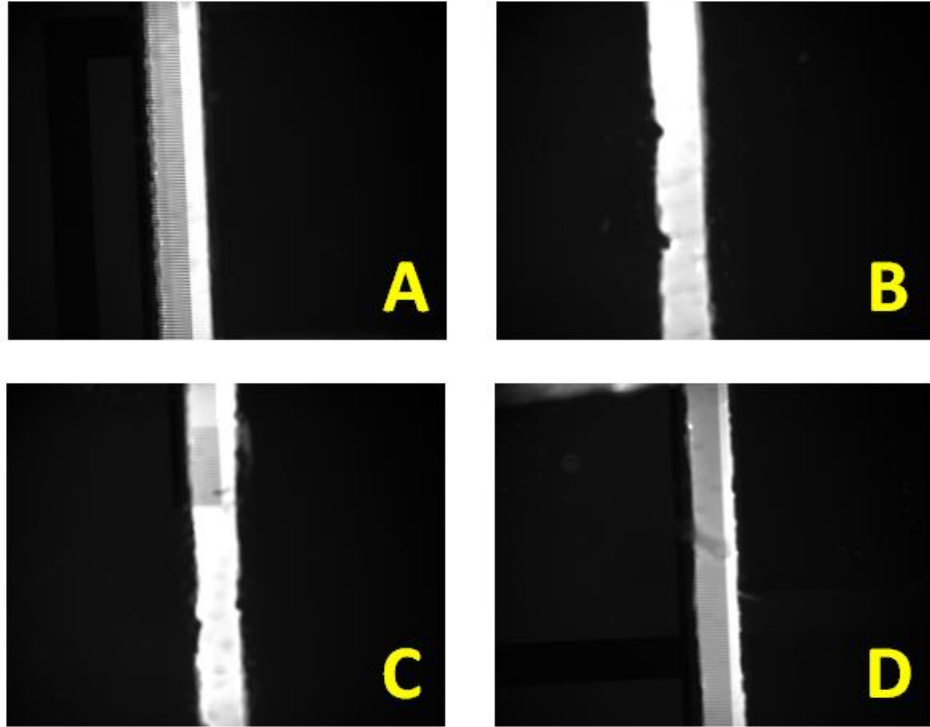


Figure 6.2 – Fluorescence microscopy images of the microfluidic channel.

To provide more quantitative analysis to check for leaks, ImageJ was used to process the images. First, a rectangular boundary was used to select the area of the image containing the channel. The “Measure” function was used to obtain the range of intensity values within the selected area. The resulting intensity values are shown in **Table 6.1** below.

Table 6.1 Mean, Minimum and Maximum Intensity Values of Fluorescence Images

Image	Mean	Min	Max
A	40163.032	1309	65535
B	35695.335	1272	65535
C	40475.292	2093	65535
D	27191.332	591	65535

The mean intensity values were used to apply a simple global threshold to each corresponding image. In **Figures 6.3A** through **6.3D**, the images are shown again with any pixel having an intensity value above the threshold highlighted. Using the threshold, it is possible to see several bright spots outside the channel that was not previously apparent. However, these bright spots are isolated and there is no evident contiguous region of brightness connecting these spots to the channel. Hence, it seems likely these bright spots are just coincidentally within the threshold and not indicative of a problematic leak.

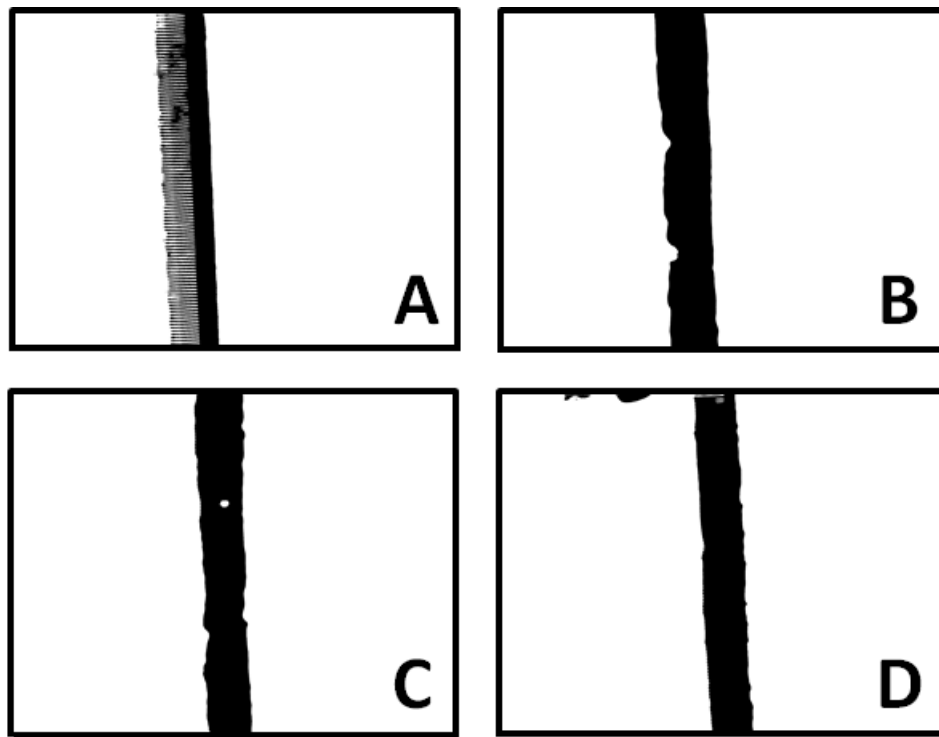


Figure 6.3 – Fluorescence images of the microfluidic channel following the application of threshold.

6.3 Flow Rate Validation

Table 6.2 Summary of the Results of the Flow Rate Validation

Flow rate (µL/min)	Run #	Expected volume (µL)	Combined mass (g)	Mass of tube (g)	Mass of water (g)	Volume of water (µL)	Actual flow rate (µL/min)	Percent error	Mean percent error (absolute value)
0.5	1	25.0	1.0132	0.9875	0.0257	25.67	0.5134	-2.68	1.46000
	2	25.0	1.0117	0.9869	0.0248	24.78	0.4956	0.88	
	3	25.0	1.0127	0.9877	0.0250	24.95	0.4990	0.20	
	4	25.0	1.0132	0.9877	0.0255	25.52	0.5104	-2.08	
1.0	1	30.0	1.0223	0.9916	0.0307	30.65	1.0217	-2.17	1.86667
	2	30.0	1.0066	0.9761	0.0305	30.46	1.0153	-1.53	
	3	30.0	1.0279	0.9973	0.0306	30.63	1.0210	-2.10	
	4	30.0	1.0220	0.9915	0.0305	30.5	1.0167	-1.67	
5.0	1	50.0	0.9732	0.9732	0.0514	51.4	5.1400	-2.80	3.00000
	2	50.0	1.0392	0.9891	0.0515	51.5	5.1500	-3.00	
	3	50.0	1.0373	0.9873	0.0516	51.6	5.1600	-3.20	
	4	50.0	0.9917	0.9917	0.0515	51.5	5.1500	-3.00	
10.0	1	50.0	1.0387	0.9876	0.0511	51.1	10.2200	-2.20	2.70000
	2	50.0	1.0445	0.9929	0.0516	51.6	10.3200	-3.20	
	3	50.0	1.0366	0.9876	0.0490	49.0	9.8000	2.00	
	4	50.0	1.0328	0.9811	0.0517	51.7	10.3400	-3.40	

The majority of the runs resulted in a negative percent error, indicating the pump overshoots and pumps more than the intended volume. The NE-1000 syringe pump uses a step motor to incrementally turn a screw which drives the plunger of the syringe. When the pump detects it has reached the desired volume and stops, there may still be some residual force that pushes more fluid through the device, causing it to overshoot the intended volume and, by extension, the flow rate. Furthermore, when viewing the means of the absolute values of the percent error, there seems to be an increasing size of error as the flow rate is increased. Again, this may be because of the mechanical limitations of the pump motor. The higher the flow rate, the faster the motor must run, causing a greater

degree of overshooting when it finally stops, resulting in greater error at the higher flow rates.

6.4 KCl Run

Figure 6.4 is the EIS spectra obtained from passing KCl through an unpacked chip at varying concentrations. As expected, an increase in the concentration of KCl ions results in a decrease in impedance. Included in **Figure 6.5** is the EIS spectra obtained by Cheng et al. in a similar experiment that utilized a packed chip and soldered electrical connections. The spectra from the current experiment exhibit the same semicircle shape of the prior experiment. Although the precise value of the impedances is different due to the differences in the experimental setup, the similarities would suggest the spring probes are well-suited for the task of providing sensitive impedimetric data for EIS applications.

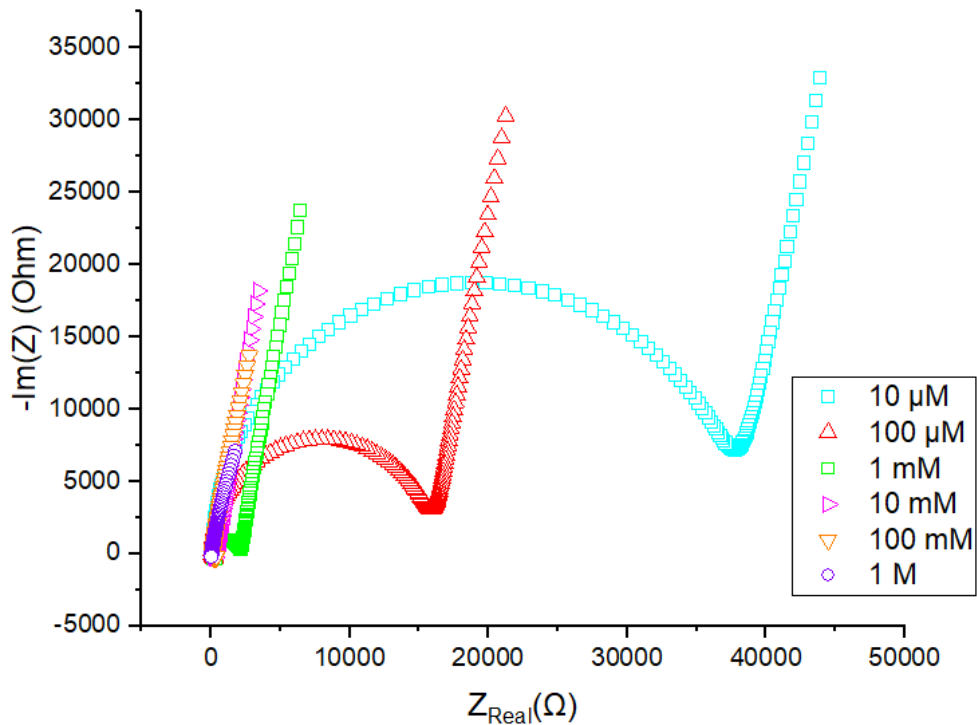


Figure 6.4 EIS spectra for multiple concentrations of KCl in unpacked chip at 100 mV.

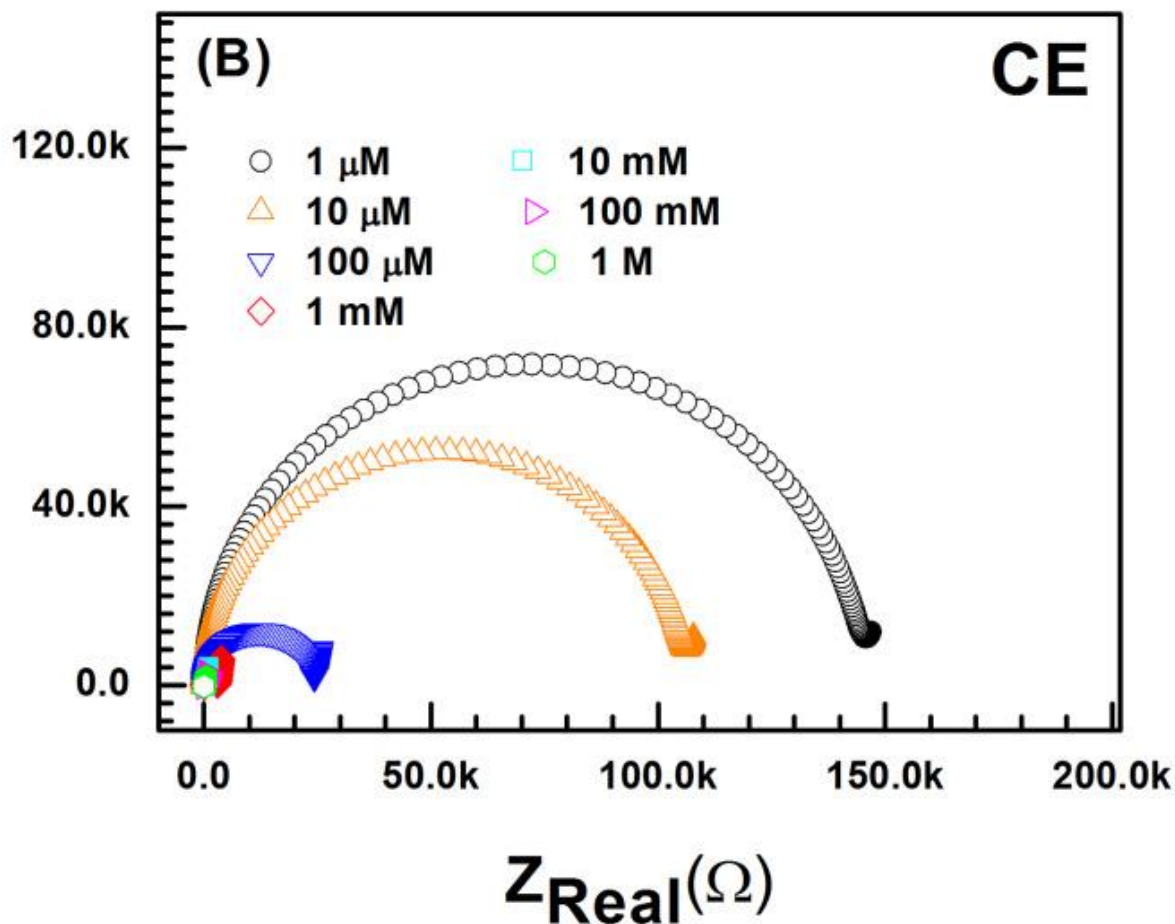


Figure 6.5 EIS spectra for multiple concentrations of KCl in a packed chip at 100 mV.

Source: Cheng, Y. H., Moura, P. A. R., Zhenglong, L., Feng, L., Arokiam, S., Yang, J., . . . Basuray, S. (2019). Effect of electrode configuration on the sensitivity of nucleic acid detection in a non-planar, flow-through, porous interdigitated electrode. *Biomicrofluidics*, 13(6), 064118. doi:10.1063/1.5126452

6.5 Target DNA Run

The probe-DNA has been coupled to the carboxylate groups on the surface of the SWCNT. The perfectly matched target-DNA will bind to this probe-DNA, which should change the ionic current to the SWCNT. This change will cause a perturbation in the total flow, which can be observed in the EIS.

The initial EIS spectra in 1 × PBS (SWCNT with probe-DNA only) and 1 × PBS washing following the passage of target-DNA were acquired. The change in the EIS spectra

for two different electrode configurations, WE and ME, are shown in **Figure 6.6** and **Figure 6.7** respectively.

As can be seen from **Figure 6.6** and **6.7**, the difference between the impedance circuits indicates the binding of the target-DNA oligo to the probe-DNA.

For comparison, the EIS spectra from a similar previous experiment conducted by Cheng et al. is included in **Figure 6.8**. The ME and WE configurations demonstrate that the binding of target-DNA to the probe-DNA causes a decrease in resistance, similar to the spectra produced by this experiment. The shape of the ME spectra is quite different from each other while the overall shape of the WE spectrum more resembles that of Cheng et al. and displays the characteristic semicircle response of the Nyquist plot. Note also that the actual values of the impedances are different for both configurations. However, this may be attributed to the differences between each experiment. The experiment of Cheng et al. used a 1 fM concentration versus a 10 nM concentration of target-DNA. Furthermore, the former utilized ethanolamine as a blocking agent to block nonreacted carboxy groups on the SWCNT and prevent nonspecific adsorption of target-DNA.

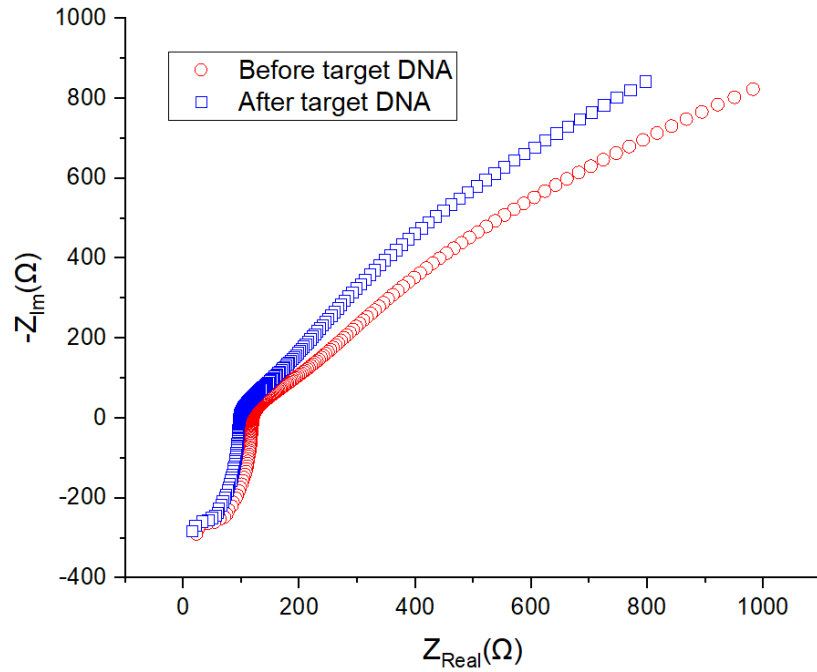


Figure 6.6 EIS spectra from target-DNA attachment to SWCNT with probe-DNA for ME configuration with a target-DNA concentration of 10 nM.

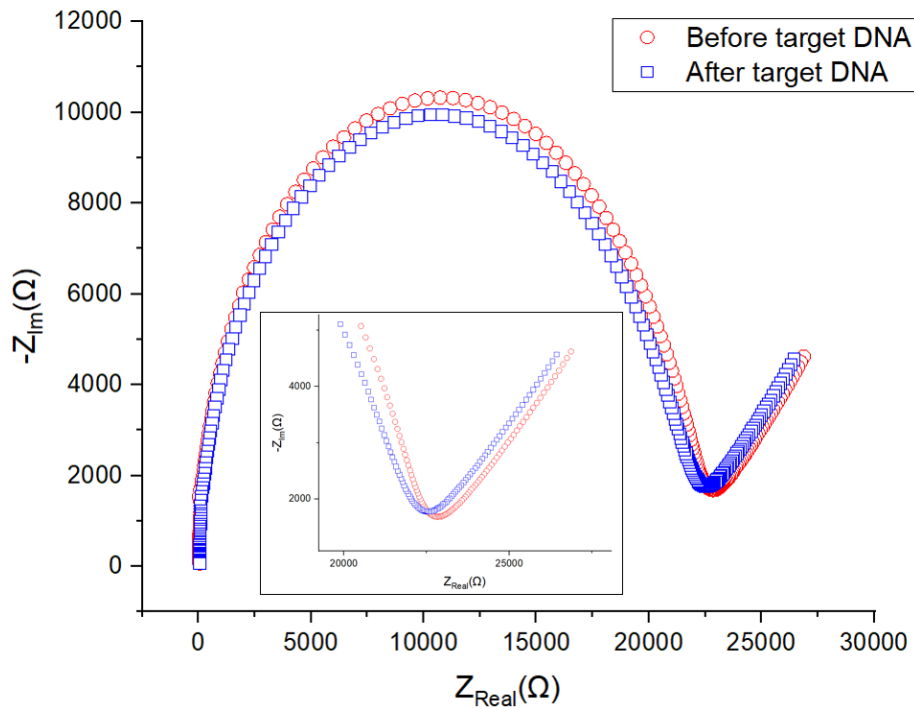


Figure 6.7 EIS spectra from target-DNA attachment to SWCNT with probe-DNA for WE configuration with a target-DNA concentration of 10 nM.

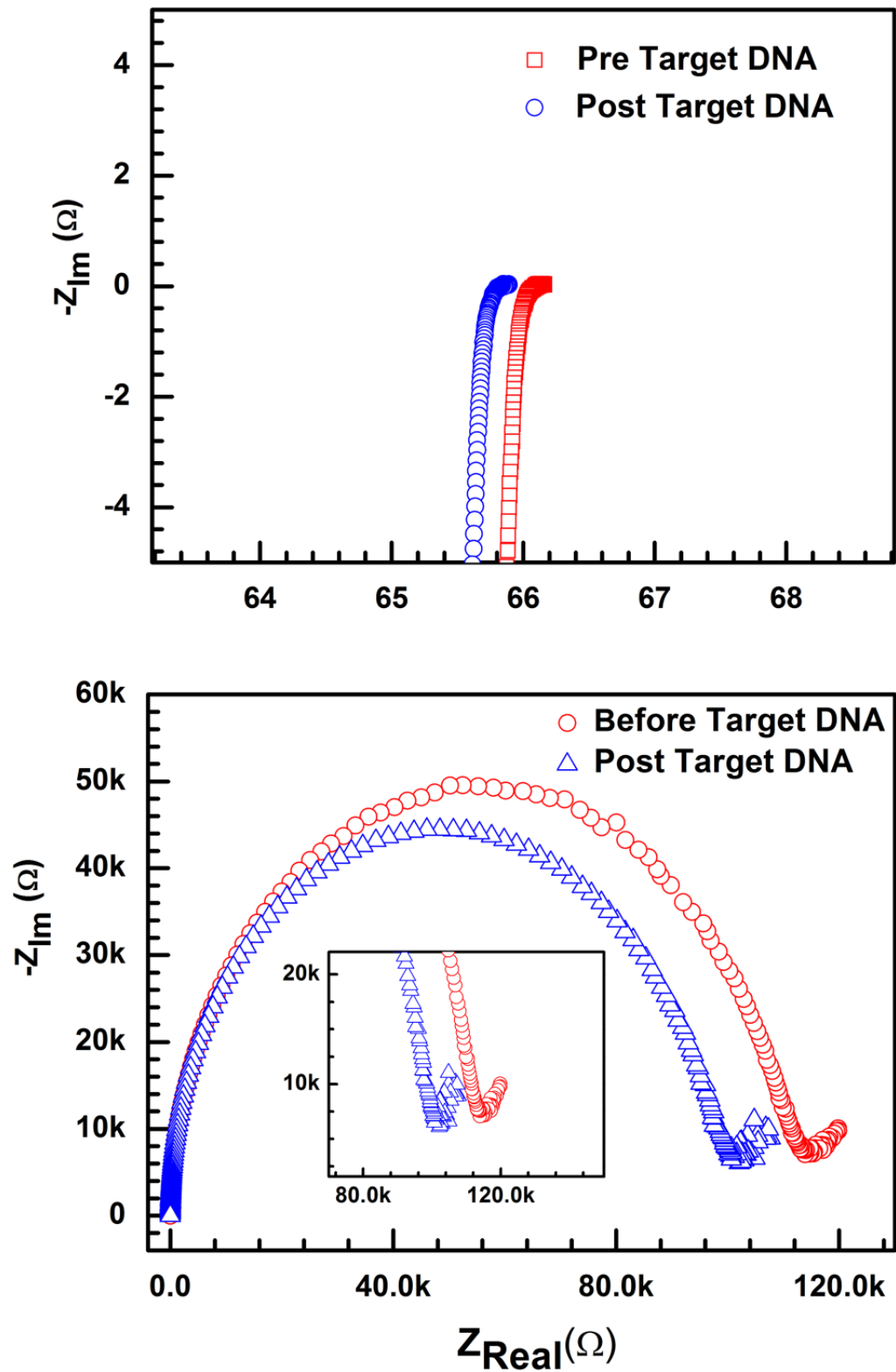


Figure 6.8 EIS spectra from target-DNA attachment to SWCNT with probe-DNA for ME (top) and WE (bottom) configuration with target-DNA concentration of 1 fM.

Source: Cheng, Y. H., Moura, P. A. R., Zhenglong, L., Feng, L., Arokiam, S., Yang, J., . . . Basuray, S. (2019). Effect of electrode configuration on the sensitivity of nucleic acid detection in a non-planar, flow-through, porous interdigitated electrode. *Biomicrofluidics*, 13(6), 064118. doi:10.1063/1.5126452

6.6 PBS Run

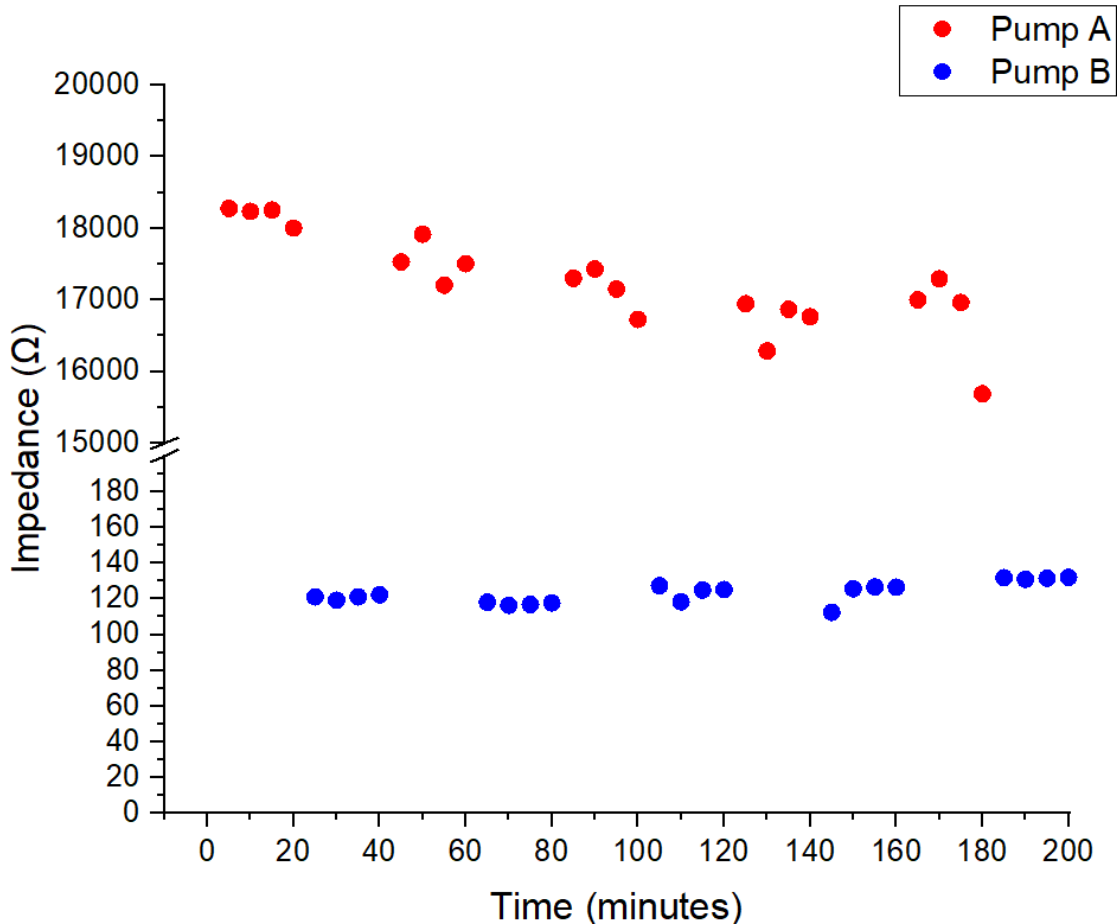


Figure 6.9 The plot of impedance over time for Run 1.

As expected, when Pump A is running the impedance is significantly higher while it is considerably lower when Pump B is running. The change from one to the other is readily apparent and well-defined. This suggests the electrical connections are sensitive and responsive enough to detect a change in solute concentration almost instantaneously.

However, there is a noticeable drift across the data points for Pump A.

To examine the effects of this drift more closely, the error was evaluated through two methods. In the first method, the mean and standard deviation of each grouping of four data points was calculated and plotted with the standard deviation being used as the error value (see **Figure 6.10**). In the second method, the two data sets (Pump A and Pump B) were normalized by dividing each grouping of four data points with their respective mean and the standard deviation was then calculated for each grouping using these normalized values. This method allows for a more direct comparison of the error in each data set by setting them at the same scale (see **Figure 6.11**).

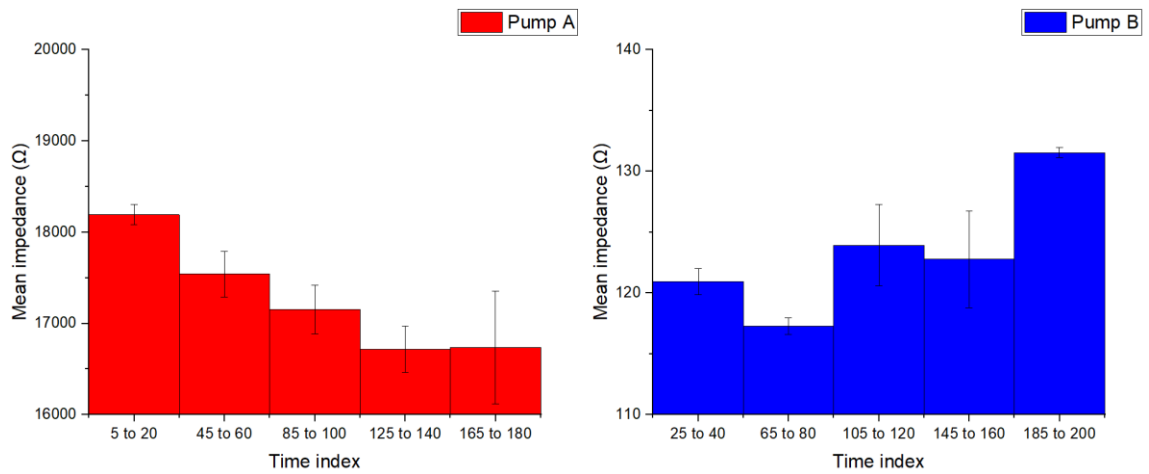


Figure 6.10 Non-normalized mean impedances and standard deviations (represented as error bars) for PBS Run 1.

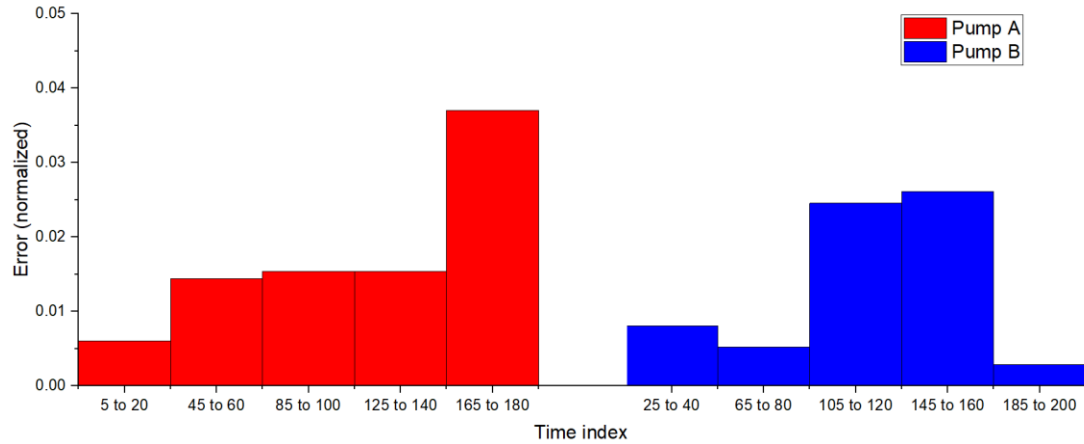


Figure 6.11 Normalized standard deviations for PBS Run 1.

The drift is more apparent in these plots, but no clear pattern emerges. The normalized error for Pump A appears to stabilize at approximately 0.015 but then increases significantly towards the end of Run 1. The normalized error for Pump B on the other hand appears to fluctuate randomly. It is possible that because the two pumps were connected by a Y-shaped connector rather than a valve that leakage occurred which caused these fluctuations.

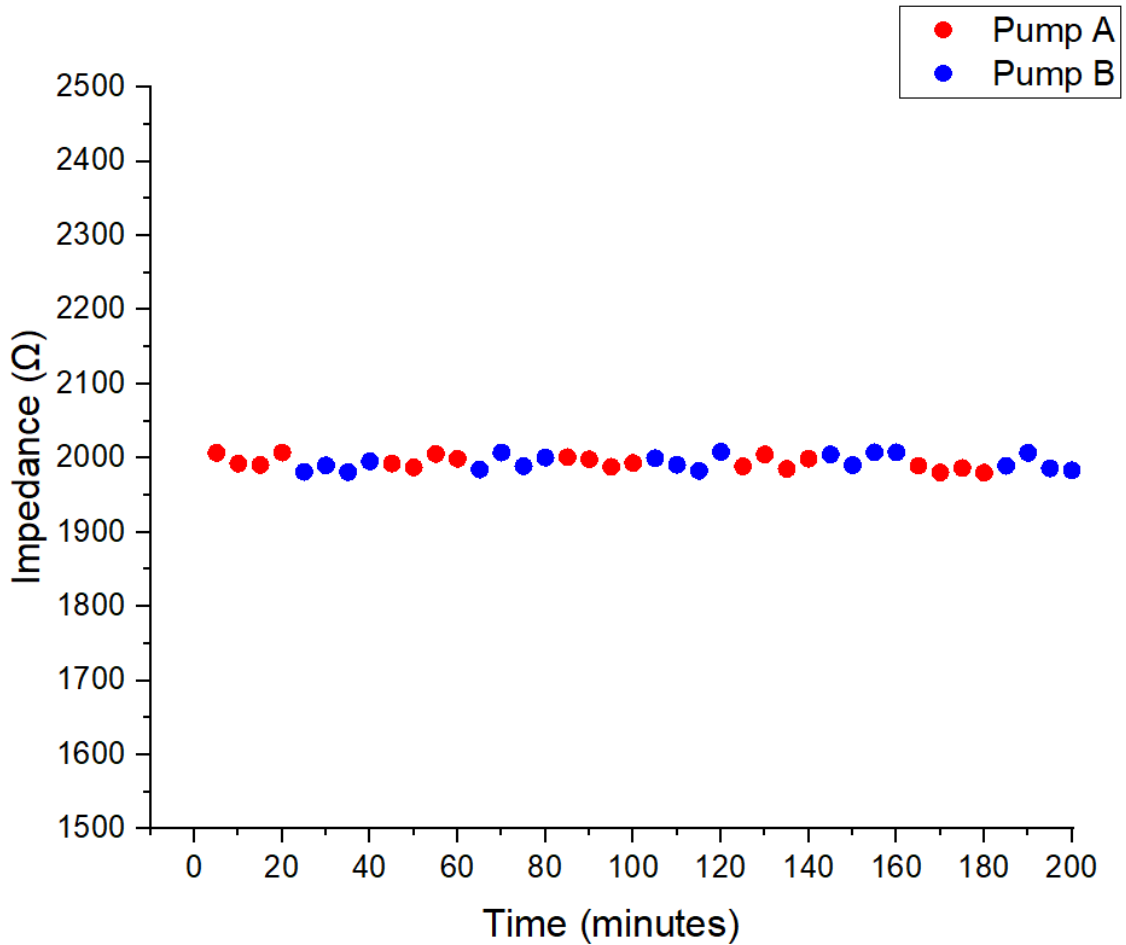


Figure 6.12 The plot of impedance over time for Run 2.

In Run 2, the concentration and flow rate for Pumps A and B are kept the same. Consequently, it was expected that the impedance values would be almost identical. As can be seen in **Figure 6.12** above, the impedance values do remain very close and are stable at approximately 2000 Ω. Once again, this suggests the electrical connections are stable and sensitive. The same two methods applied to Run 1 were used to evaluate the error for Run 2 and their respective plots are shown in **Figure 6.13** and **Figure 6.14**.

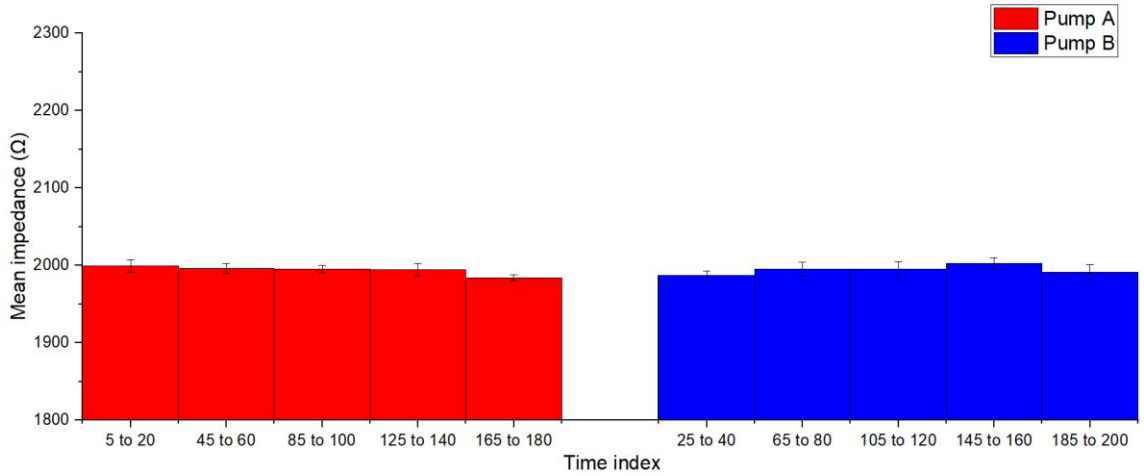


Figure 6.13 Non-normalized mean impedances and standard deviations (represented as error bars) for PBS Run 2.

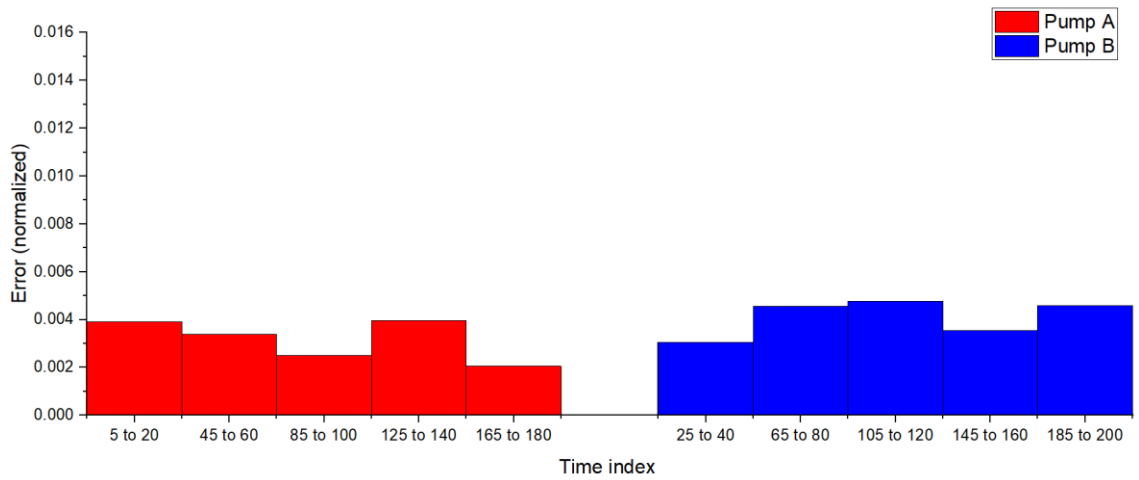


Figure 6.14 Normalized standard deviations for PBS Run 2.

The plot of the mean impedance further reinforces that the system is stable and correctly measures that the impedance is the same for each pump. The plot of the normalized error also shows stability and indicates the error is comparatively small, ranging from approximately 0.002 to 0.004.

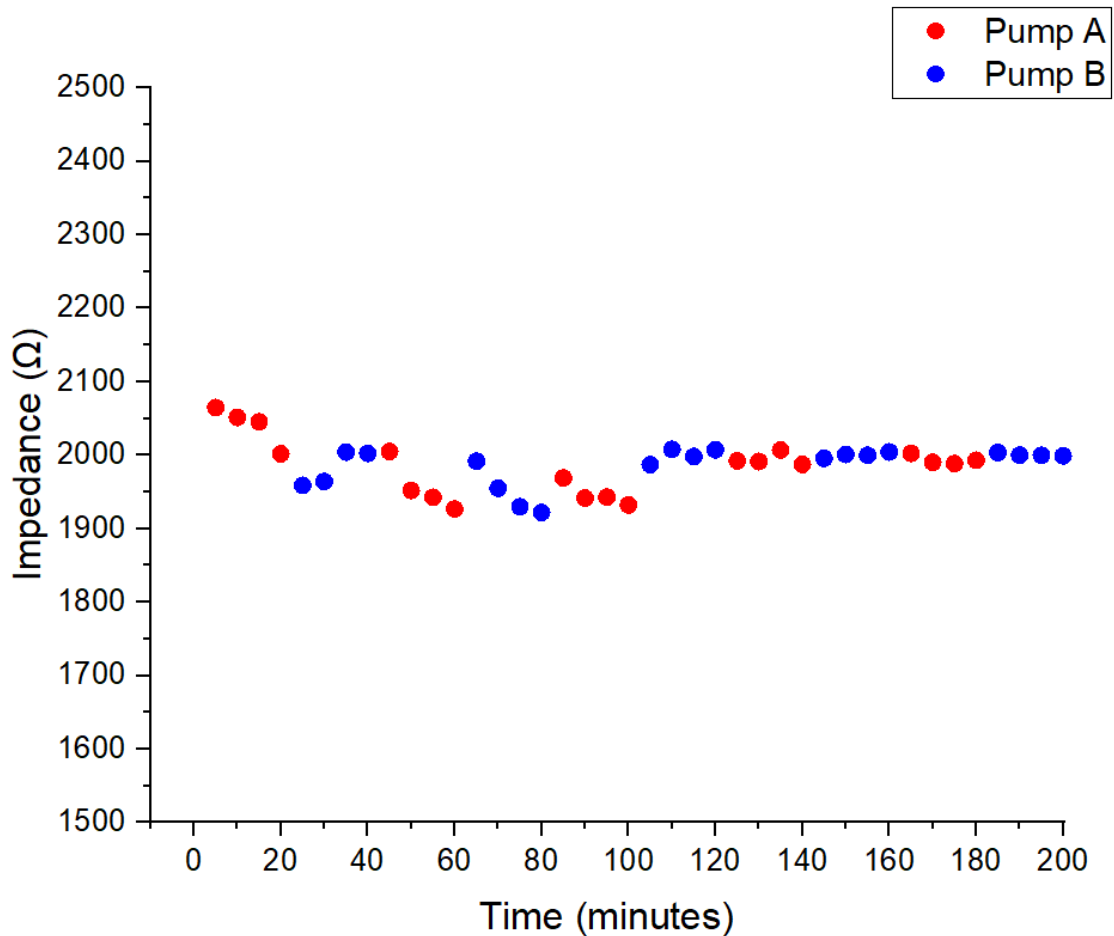


Figure 6.15 The plot of impedance over time for Run 3.

In Run 3, the concentration was kept the same between the two pumps, but the flow rates varied. It is expected that, similar to Run 2, the impedance measurements would not vary significantly from one pump to the other as the flow rate should have minimal effect on impedance. Furthermore, the actual values of the impedance should be approximately the same as the impedance observed in Run 2 as the concentration is the same between the two runs. As expected, the impedance throughout the 200-minute run ranges between 1900 and 2100 Ω . However, there appears to be a visibly higher degree of variation in the first 100 minutes of the run before the impedance values stabilize closer to 2000 Ω . This may

be the result of not completely flushing the channel prior to taking the first sets of readings, resulting in a noticeable drift in the EIS spectra. As the pumping continues and residual solution is completely flushed, the impedance becomes more stable.

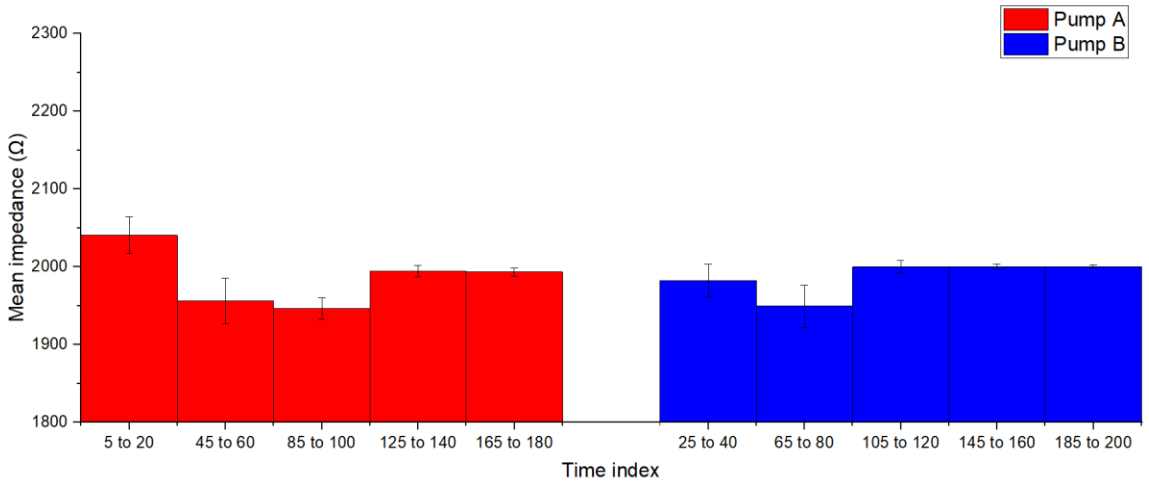


Figure 6.16 Non-normalized mean impedances and standard deviations (represented as error bars) for PBS Run 3.

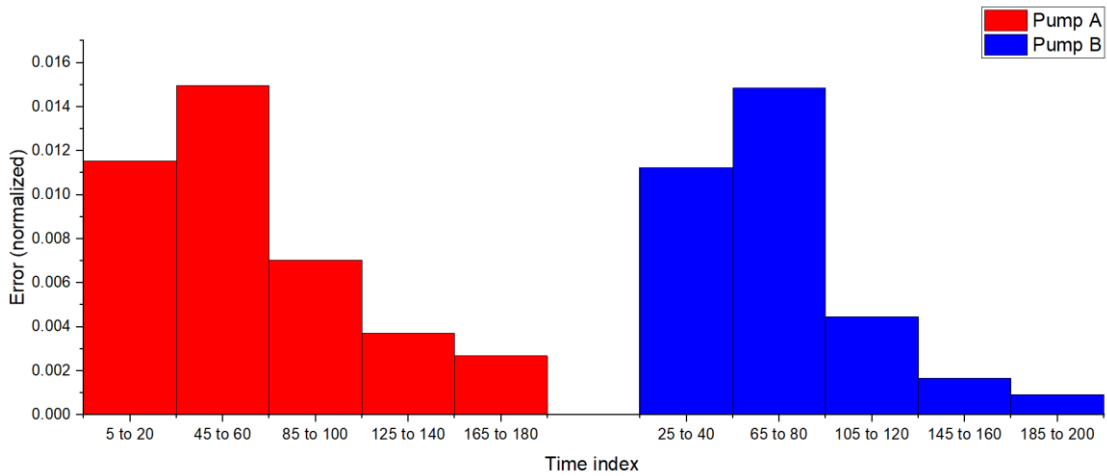


Figure 6.17 Normalized standard deviations for PBS Run 3.

Note that the scales for the plots in **Figures 6.16** and **6.17** are the same as those of **Figures 6.13** and **6.14** so it is possible to compare the two runs. In **Figure 6.16**, the means of the signal are all approximately 2000 Ω similar to the corresponding plot in Run 2 (see

Figure 6.13). In **Figure 6.17**, it can be seen the error for this run reaches a maximum at around the 1-hour mark before steadily decreasing in both pumps. This lends credence to the possibility that because the pumps are switching, it takes time for the system to be completely flushed and produce a steady signal again.

CHAPTER 7

CONCLUSION

Through the application of 3D printing, a cost-effective and easily fabricated chip-to-world interface has been realized. Except for the spring probes, the resulting design can be assembled simply snapping and fitting together the various components without the need for fasteners or adhesives.

The experiments conducted have demonstrated that the overall design is robust enough and the electrical interconnects stable and sensitive enough to be used for EIS applications. Firstly, the visual inspection of the food colorant run revealed no sign of leakage. Both visual inspection of the fluorescence microscopy images, and the application of a simple global threshold, further confirm the lack of any leakage. The flow rate produced by the syringe pump appeared to be significantly different from that of the input flow rate. This can likely be attributed to dead volume and emphasizes the need to improve the fluidic interconnects where this dead volume likely resides. The KCL and target-DNA runs also yielded EIS spectra that closely resemble those produced from devices using the standard soldered connections, indicating they can be used for sensing electrochemical analytes. The PBS runs further demonstrated the reliability of the electrical connections and were able to immediately respond to changes in electrolyte concentration. However, from these runs it was also seen that the system likely needs to be flushed thoroughly and may require additional time before reaching a steady-state that can be measured.

Additionally, the LabVIEW program was used to control the operation of the syringe pump throughout all the experiments, as mentioned earlier. With each use the

pumping parameters input to the LabVIEW program were confirmed against the syringe pump's digital display, demonstrating successful communication. The LabVIEW program also provided real-time information about the pumping process and was able to not only initiate a pumping sequence but also terminate automatically without additional user input.

CHAPTER 8

FUTURE WORK

There are many aspects of the current platform that could be expanded upon or otherwise improved in future work. First and foremost, the LabVIEW program could be developed to control additional fluidic components. The most obvious addition would be of a computer-controlled valve and using LabVIEW to switch between various ports. This would further streamline the experimental protocol by allowing multiple syringes to be connected to a single microfluidic device by a valve. For example, in an EIS experiment it is necessary to clear the microfluidic channel with a wash before passing through a sample for analysis. Rather than have to disconnect and reconnect tubing manually, there could be two or more syringe pumps loaded in advance with different samples, reagents or wash fluids. With the proper protocol, the LabVIEW program could switch a valve to allow flow from a dedicated “wash” pump, then upon completion, turn the valve to allow flow from a pump containing “Sample #1”. Then once the desired volume of Sample #1 is dispensed, the program could switch to the wash pump, then to Sample #2 and so on. This would significantly reduce or even eliminate the need for human intervention beyond the need to operate whatever equipment is used actually to acquire data. This, in turn, would allow non-experts to contribute more in the laboratory space as they could focus on the task of acquiring and analyzing data rather than manually handling and reconfiguring a complicated mess of tubing and pumps.

Secondly, the LabVIEW program could be extended to include control over the electrical connections between the chip and peripheral analysis machines. This would make it possible to switch between pairs of electrodes pads on the chip to gather EIS data. The

ability to change configurations without having to rewire the device manually would improve turnaround time.

In terms of the physical components, the spring probes have proven to be a reliable means of making reversible connections to the electrode contact pads. The area which can be improved however is in the fluidic interconnects. The current design uses barbed fluid ports bonded to the chip's fluid inlet with adhesive and tubing to connect the port to the syringe pump. Ideally, the fluidic connections would be fully reversible, eliminating the need for permanent adhesives much like how the incorporation of spring probes eliminated the need for soldering wires directly to the electrode pads. Any such design would have to consider the issue of dead volume forming at the interface between the macroscale pump and tubing with the microscale of the fluidic channel.

APPENDIX A

LABVIEW BLOCK DIAGRAMS

Figures A.1 to A.3 show magnified views of various modules of the LabVIEW block diagram.

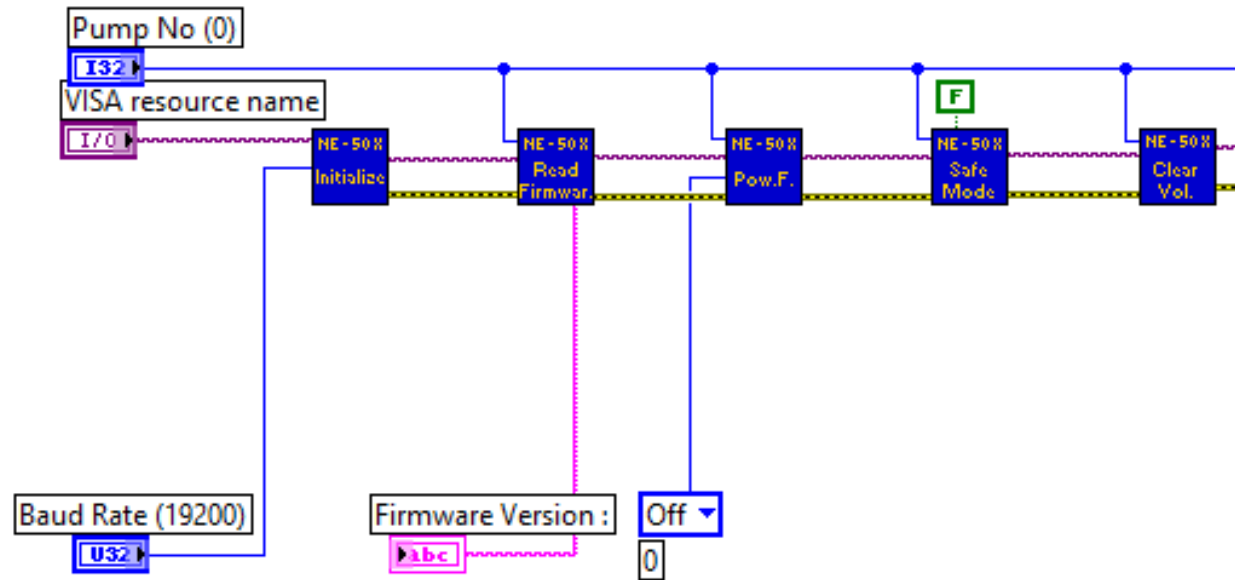


Figure A.1 Magnified view of the initialization module.

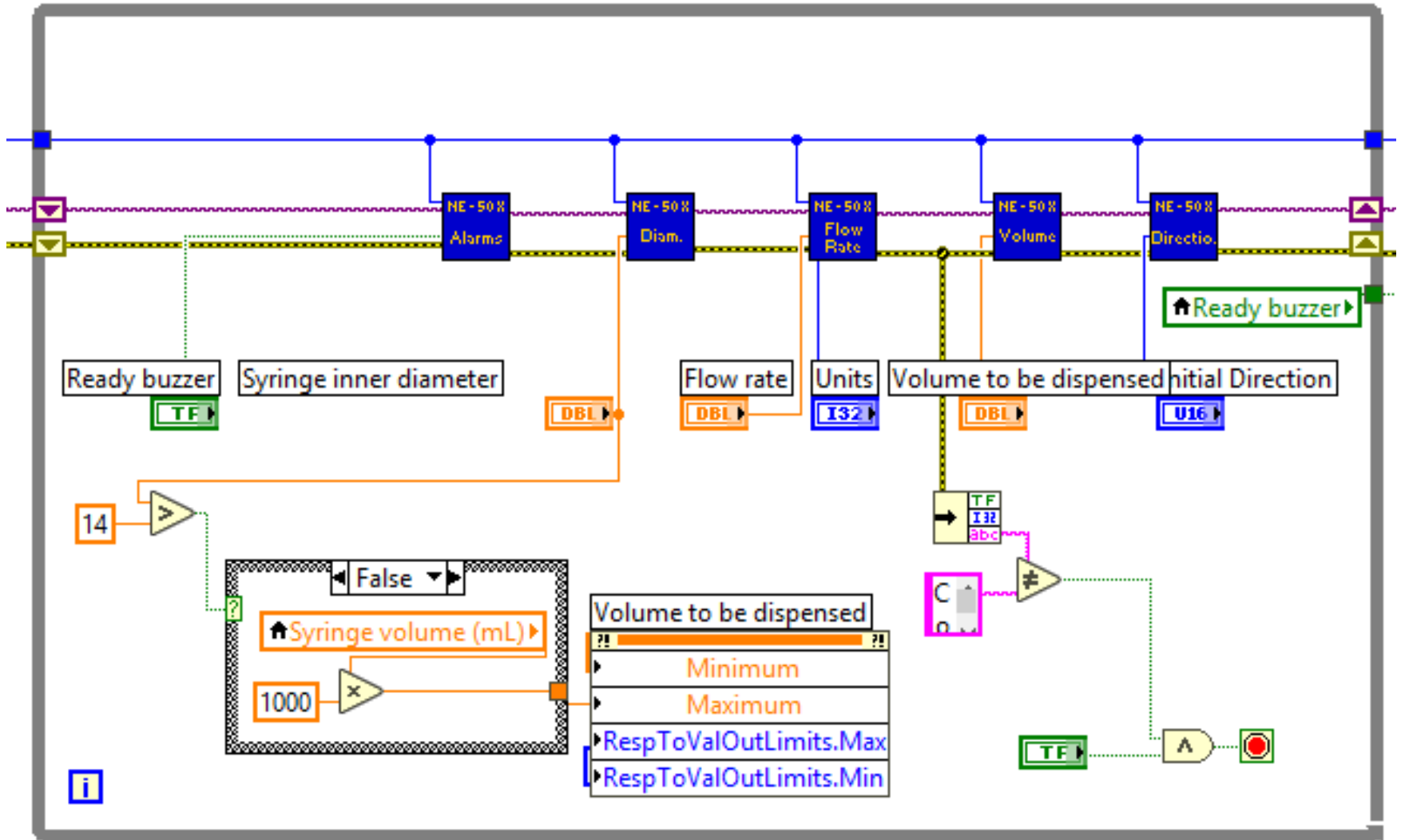


Figure A.2 Magnified view of parameters module.

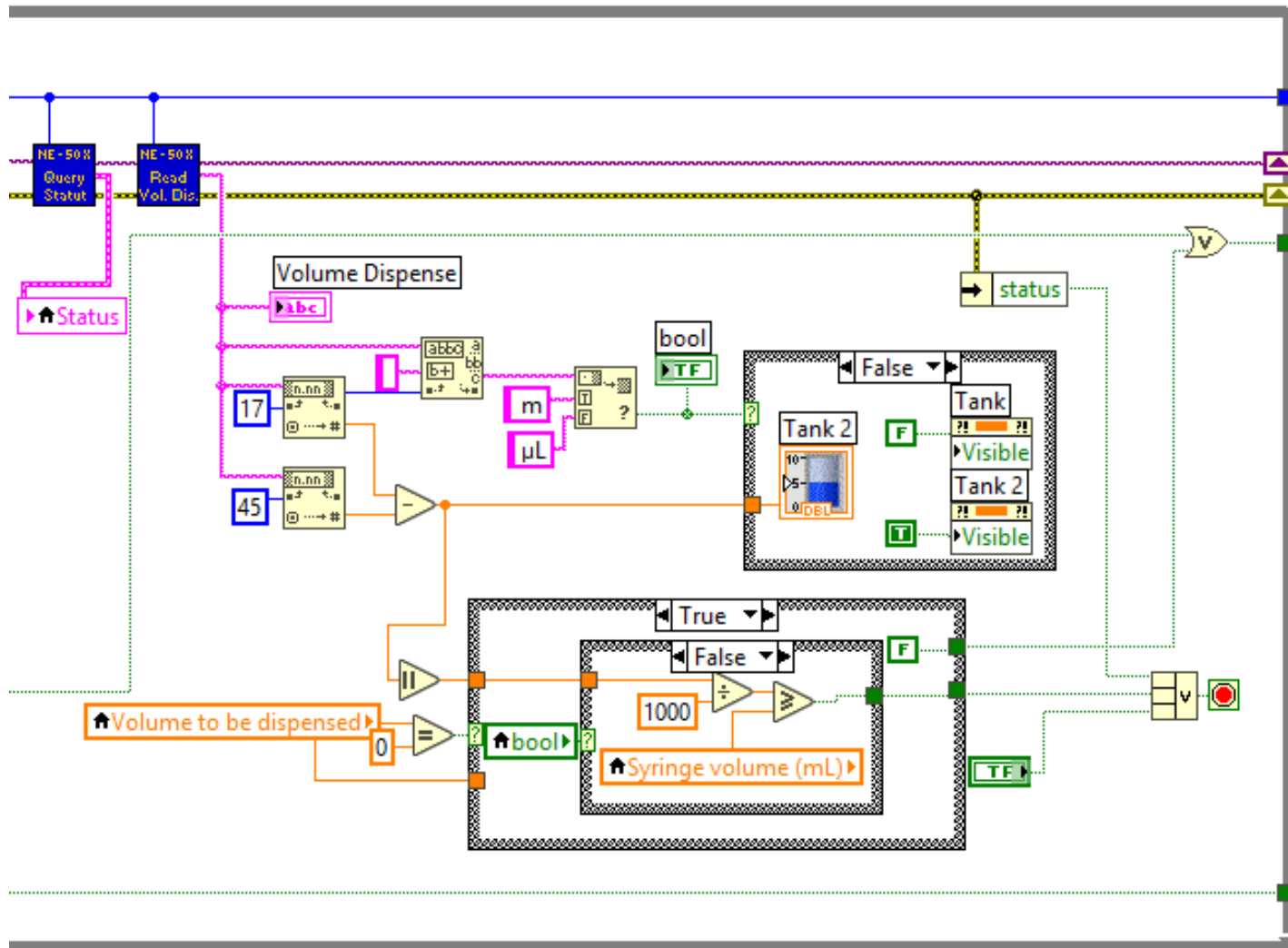


Figure A.4 Magnified view of the second half of the operations module.

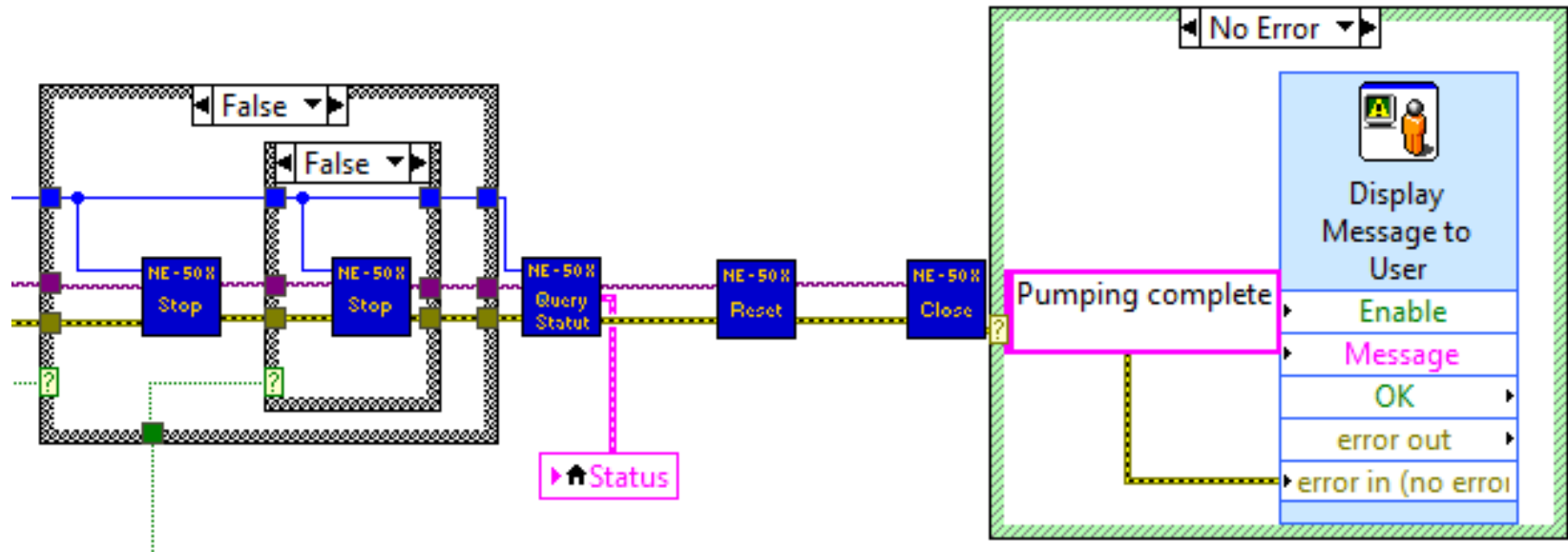


Figure A.5 Magnified view of termination module.

REFERENCES

- Barbier, V., Tatoulian, M., Li, H., Arefi-Khonsari, F., Ajdari, A., & Tabeling, P. (2006). Stable Modification of PDMS Surface Properties by Plasma Polymerization: Application to the Formation of Double Emulsions in Microfluidic Systems. *Langmuir*, 22(12), 5230-5232. doi:10.1021/la053289c
- Bassous, E., Taub, H. H., & Kuhn, L. (1977). Ink jet printing nozzle arrays etched in silicon. *Applied Physics Letters*, 31(2), 135-137. doi:10.1063/1.89587
- Chen, C. H., Lu, Y., Sin, M. L., Mach, K. E., Zhang, D. D., Gau, V., . . . Wong, P. K. (2010). Antimicrobial susceptibility testing using high surface-to-volume ratio microchannels. *Anal Chem*, 82(3), 1012-1019. doi:10.1021/ac9022764
- Cheng, C., Chang, Y.-P., & Chu, Y.-H. (2011). ChemInform Abstract: Biomolecular Interactions and Tools for Their Recognition: Focus on the Quartz Crystal Microbalance and Its Diverse Surface Chemistries and Applications. *Chemical Society Reviews*, 41, 1947-1971. doi:10.1039/c1cs15168a
- Cheng, Y. H., Moura, P. A. R., Zhenglong, L., Feng, L., Arokiam, S., Yang, J., . . . Basuray, S. (2019). Effect of electrode configuration on the sensitivity of nucleic acid detection in a non-planar, flow-through, porous interdigitated electrode. *Biomicrofluidics*, 13(6), 064118. doi:10.1063/1.5126452
- Chin, C. D., Linder, V., & Sia, S. K. (2007). Lab-on-a-chip devices for global health: past studies and future opportunities. *Lab Chip*, 7(1), 41-57. doi:10.1039/b611455e
- Choi, S., & Chae, J. (2010). A Physisorbed Interface Design of Biomolecules for Selective and Sensitive Protein Detection. *Journal of The Association for Laboratory Automation*, 15, 172-178. doi:10.1016/j.jala.2009.09.002

- Chung, A. J., Kim, D., & Erickson, D. (2008). Electrokinetic microfluidic devices for rapid, low power drug delivery in autonomous microsystems. *Lab Chip*, 8(2), 330-338. doi:10.1039/b713325a
- Chung, J., Hwang, H. Y., Chen, Y., & Lee, T. Y. (2018). Microfluidic packaging of high-density CMOS electrode array for lab-on-a-chip applications. *Sensors and Actuators B: Chemical*, 254, 542-550.
doi:<https://doi.org/10.1016/j.snb.2017.07.122>
- Churski, K., Michalski, J., & Garstecki, P. (2010). Droplet on demand system utilizing a computer controlled microvalve integrated into a stiff polymeric microfluidic device. *Lab Chip*, 10(4), 512-518. doi:10.1039/b915155a
- Convery, N., & Gadegaard, N. (2019). 30 years of microfluidics. *Micro and Nano Engineering*, 2, 76-91. doi:<https://doi.org/10.1016/j.mne.2019.01.003>
- Dittrich, P. S., Tachikawa, K., & Manz, A. (2006). Micro total analysis systems. Latest advancements and trends. *Anal Chem*, 78(12), 3887-3908. doi:10.1021/ac0605602
- Drain, P. K., Hyle, E. P., Noubary, F., Freedberg, K. A., Wilson, D., Bishai, W. R., . . . Bassett, I. V. (2014). Diagnostic point-of-care tests in resource-limited settings. *Lancet Infect Dis*, 14(3), 239-249. doi:10.1016/s1473-3099(13)70250-0
- Ghafar-Zadeh, E., Sawan, M., & Therriault, D. (2009). A Microfluidic Packaging Technique for Lab-on-Chip Applications. *IEEE Transactions on Advanced Packaging*, 32(2), 410-416. doi:10.1109/TADVP.2008.920655
- Gomez, F. A. (2013). The future of microfluidic point-of-care diagnostic devices. *Bioanalysis*, 5(1), 1-3. doi:10.4155/bio.12.307

- Guo, X. (2012). Surface plasmon resonance based biosensor technique: a review. *J Biophotonics*, 5(7), 483-501. doi:10.1002/jbio.201200015
- Guo, X., Kulkarni, A., Doepke, A., Halsall, H. B., Iyer, S., & Heineman, W. R. (2012). Carbohydrate-based label-free detection of Escherichia coli ORN 178 using electrochemical impedance spectroscopy. *Anal Chem*, 84(1), 241-246. doi:10.1021/ac202419u
- Hettiarachchi, K., Talu, E., Longo, M. L., Dayton, P. A., & Lee, A. P. (2007). On-chip generation of microbubbles as a practical technology for manufacturing contrast agents for ultrasonic imaging. *Lab on a Chip*, 7(4), 463-468. doi:10.1039/B701481N
- Huang, S.-B., Wu, M.-H., Cui, Z., Cui, Z., & Lee, G.-B. (2008). A membrane-based serpentine-shape pneumatic micropump with pumping performance modulated by fluidic resistance. *Journal of Micromechanics and Microengineering*, 18, 045008. doi:10.1088/0960-1317/18/4/045008
- Jeong, O., & Konishi, S. (2008). Fabrication of a peristaltic micro pump with novel cascaded actuators. *Journal of Micromechanics and Microengineering*, 18, 025022. doi:10.1088/0960-1317/18/2/025022
- Jr, W. (2001). Microelectronics: Its unusual origin and personality. *Electron Devices, IEEE Transactions on*, 48, 2457-2467. doi:10.1109/16.960368
- Kaigala, G. V., Hoang, V. N., & Backhouse, C. J. (2008). Electrically controlled microvalves to integrate microchip polymerase chain reaction and capillary electrophoresis. *Lab Chip*, 8(7), 1071-1078. doi:10.1039/b802853b

- Kilby, J. (2000). The integrated circuit's early history. *Proceedings of the IEEE*, 88, 109-111. doi:10.1109/5.811607
- Kim, J., Chen, D., & Bau, H. H. (2009). An automated, pre-programmed, multiplexed, hydraulic microvalve. *Lab Chip*, 9(24), 3594-3598. doi:10.1039/b914865e
- Kim, J., Junkin, M., Kim, D.-H., Kwon, S., Shin, Y. S., Wong, P. K., & Gale, B. K. (2009). Applications, techniques, and microfluidic interfacing for nanoscale biosensing. *Microfluidics and Nanofluidics*, 7(2), 149-167. doi:10.1007/s10404-009-0431-8
- Kuo, J. S., & Chiu, D. T. (2011). Controlling mass transport in microfluidic devices. *Annu Rev Anal Chem (Palo Alto Calif)*, 4, 275-296. doi:10.1146/annurev-anchem-061010-113926
- Lathrop, J. (2013). The Diamond Ordnance Fuze Laboratory's Photolithographic Approach to Microcircuits. *IEEE Annals of the History of Computing, Volume 35*, 48. doi:10.1109/MAHC.2011.83
- Lee, M.-K., Lee, T. J., Choi, H. W., Shin, S. J., Park, J. Y., & Lee, S. J. (2014). A universal system for reliable probing of electrochemical lab-on-a-chip devices. *Sensors (Basel, Switzerland)*, 14(1), 944-956. doi:10.3390/s140100944
- Liu, Y., Schweizer, L., Wang, W., Reuben, R., Schweizer, M., & Shu, W. (2013). Label-free and real-time monitoring of yeast cell growth by the bending of polymer microcantilever biosensors. *Sensors and Actuators B: Chemical*, 178, 621-626. doi:10.1016/j.snb.2012.12.111
- Luka, G., Ahmadi, A., Najjaran, H., Alocilja, E., DeRosa, M., Wolthers, K., . . . Hoorfar, M. (2015). Microfluidics Integrated Biosensors: A Leading Technology towards

- Lab-on-a-Chip and Sensing Applications. *Sensors (Basel)*, 15(12), 30011-30031.
doi:10.3390/s151229783
- Mansur, E., Ye, M., Wang, Y., & Dai, Y. (2008). A State-of-the-Art Review of Mixing in Microfluidic Mixers. *Chinese Journal of Chemical Engineering*, 16, 503-516.
doi:10.1016/S1004-9541(08)60114-7
- Manz, A., Graber, N., & Widmer, H. M. (1990). Miniaturized total chemical analysis systems: A novel concept for chemical sensing. *Sensors and Actuators B: Chemical*, 1(1), 244-248. doi:[https://doi.org/10.1016/0925-4005\(90\)80209-I](https://doi.org/10.1016/0925-4005(90)80209-I)
- Mark, D., Haeberle, S., Roth, G., von Stetten, F., & Zengerle, R. (2010). Microfluidic lab-on-a-chip platforms: requirements, characteristics and applications. *Chemical Society Reviews*, 39(3), 1153-1182. doi:10.1039/B820557B
- Mohammed, M., Haswell, S., & Gibson, I. (2015). Lab-on-a-chip or Chip-in-a-lab: Challenges of Commercialization Lost in Translation. *Procedia Technology*, 20, 54-59. doi:10.1016/j.protcy.2015.07.010
- Nayak, S., Blumenfeld, N. R., Laksanasopin, T., & Sia, S. K. (2017). Point-of-Care Diagnostics: Recent Developments in a Connected Age. *Analytical chemistry*, 89(1), 102-123. doi:10.1021/acs.analchem.6b04630
- Ng, A. H. C., & Wheeler, A. R. (2015). Next-Generation Microfluidic Point-of-Care Diagnostics. *Clinical Chemistry*, 61(10), 1233-1234.
doi:10.1373/clinchem.2015.240226
- Nguyen, N.-T., & Wu, Z. (2005). Micromixers—A Review. *Journal of Micromechanics and Microengineering*, 15, 1. doi:10.1088/0960-1317/15/2/R01

- Posthuma-Trumpie, G. A., Korf, J., & van Amerongen, A. (2009). Lateral flow (immuno)assay: its strengths, weaknesses, opportunities and threats. A literature survey. *Anal Bioanal Chem*, 393(2), 569-582. doi:10.1007/s00216-008-2287-2
- Reynolds, O. (1883). XXIX. An experimental investigation of the circumstances which determine whether the motion of water shall be direct or sinuous, and of the law of resistance in parallel channels. *Philosophical Transactions of the Royal Society of London*, 174, 935-982. doi:doi:10.1098/rstl.1883.0029
- Rohde, C. B., Zeng, F., Gonzalez-Rubio, R., Angel, M., & Yanik, M. F. (2007). Microfluidic system for on-chip high-throughput whole-animal sorting and screening at subcellular resolution. *Proc Natl Acad Sci U S A*, 104(35), 13891-13895. doi:10.1073/pnas.0706513104
- Ryu, K., Chung, S. K., & Cho, S. K. (2010). Micropumping by an Acoustically Excited Oscillating Bubble for Automated Implantable Microfluidic Devices. *JALA*, 15, 163-171. doi:10.1016/j.jala.2010.01.012
- Schneider, G. (2018). Automating drug discovery. *Nature Reviews Drug Discovery*, 17(2), 97-113. doi:10.1038/nrd.2017.232
- Sharma, S., Zapatero-Rodríguez, J., Estrela, P., & O'Kennedy, R. (2015). Point-of-Care Diagnostics in Low Resource Settings: Present Status and Future Role of Microfluidics. *Biosensors*, 5(3), 577-601. doi:10.3390/bios5030577
- Shi, W., & Ma, Z. (2011). A novel label-free amperometric immunosensor for carcinoembryonic antigen based on redox membrane. *Biosens Bioelectron*, 26(6), 3068-3071. doi:10.1016/j.bios.2010.11.048

- Sista, R., Hua, Z., Thwar, P., Sudarsan, A., Srinivasan, V., Eckhardt, A., . . . Pamula, V. (2008). Development of a digital microfluidic platform for point of care testing. *Lab Chip*, 8(12), 2091-2104. doi:10.1039/b814922d
- Squires, T. M., & Quake, S. R. (2005). Microfluidics: Fluid physics at the nanoliter scale. *Reviews of Modern Physics*, 77(3), 977-1026. doi:10.1103/RevModPhys.77.977
- Strutt, J. W. (1879). VI. On the capillary phenomena of jets. *Proceedings of the Royal Society of London*, 29(196-199), 71-97. doi:doi:10.1098/rspl.1879.0015
- Sweet, R. G. (1965). High Frequency Recording with Electrostatically Deflected Ink Jets. *Review of Scientific Instruments*, 36(2), 131-136. doi:10.1063/1.1719502
- Temiz, Y., Lovchik, R. D., Kaigala, G. V., & Delamarche, E. (2015). Lab-on-a-chip devices: How to close and plug the lab? *Microelectronic Engineering*, 132, 156-175. doi:<https://doi.org/10.1016/j.mee.2014.10.013>
- Terry, S. C., Jerman, J. H., & Angell, J. B. (1979). A gas chromatographic air analyzer fabricated on a silicon wafer. *IEEE Transactions on Electron Devices*, 26(12), 1880-1886. doi:10.1109/T-ED.1979.19791
- Tudos, A. J., Besselink, G. J., & Schasfoort, R. B. (2001). Trends in miniaturized total analysis systems for point-of-care testing in clinical chemistry. *Lab Chip*, 1(2), 83-95. doi:10.1039/b106958f
- Unger, M. A., Chou, H. P., Thorsen, T., Scherer, A., & Quake, S. R. (2000). Monolithic microfabricated valves and pumps by multilayer soft lithography. *Science*, 288(5463), 113-116. doi:10.1126/science.288.5463.113

- Wang, S., Inci, F., De Libero, G., Singhal, A., & Demirci, U. (2013). Point-of-care assays for tuberculosis: role of nanotechnology/microfluidics. *Biotechnol Adv*, *31*(4), 438-449. doi:10.1016/j.biotechadv.2013.01.006
- Ward, K., & Fan, Z. H. (2015). Mixing in microfluidic devices and enhancement methods. *J Micromech Microeng*, *25*(9). doi:10.1088/0960-1317/25/9/094001
- Whitesides, G. M. (2006). The origins and the future of microfluidics. *Nature*, *442*(7101), 368-373. doi:10.1038/nature05058
- Xu, Y., Wu, X., Guo, X., Kong, B., Zhang, M., Qian, X., . . . Sun, W. (2017). The Boom in 3D-Printed Sensor Technology. *Sensors (Basel, Switzerland)*, *17*(5), 1166. doi:10.3390/s17051166
- Yager, P., Domingo, G. J., & Gerdes, J. (2008). Point-of-care diagnostics for global health. *Annu Rev Biomed Eng*, *10*, 107-144. doi:10.1146/annurev.bioeng.10.061807.160524
- Yager, P., Edwards, T., Fu, E., Helton, K., Nelson, K., Tam, M. R., & Weigl, B. H. (2006). Microfluidic diagnostic technologies for global public health. *Nature*, *442*(7101), 412-418. doi:10.1038/nature05064
- Yang, X., Sun, Z., Tian, F., Jia, G., Yang, J., & Hu, X. (2018). A lateral flow immunochromatographic strip test for rapid detection of hexoestrol in fish samples. *Royal Society open science*, *5*(8), 180504-180504. doi:10.1098/rsos.180504
- Yildiz-Ozturk, E., & Yesil-Celiktas, O. (2015). Diffusion phenomena of cells and biomolecules in microfluidic devices. *Biomicrofluidics*, *9*(5), 052606. doi:10.1063/1.4923263

Zelada-Guillen, G. A., Tweed-Kent, A., Niemann, M., Goring, H. U., Riu, J., & Rius, F. X. (2013). Ultrasensitive and real-time detection of proteins in blood using a potentiometric carbon-nanotube aptasensor. *Biosens Bioelectron*, *41*, 366-371. doi:10.1016/j.bios.2012.08.055